A comparative analysis of capacity and non-capacity formulations for the simulation of unsteady flows over finite-depth erodible beds

S. Martínez-Aranda*, J. Murillo, P. García-Navarro

LIFTEC-CSIC, University of Zaragoza, Spain

Abstract

Finite-depth sediment layers are common in natural water bodies. The presence of underlying bedrock strata covered by erodible bed layers is ubiquitous in rivers and estuaries. In the last years, the development of models based on the non-capacity sediment transport assumption, also called non-equilibrium assumption, has offered a new theoretical background to deal with complex non-erodible bed configurations and the associated numerical problems. Bedload non-capacity sediment transport models consider that the actual solid transport state can be different from the equilibrium state and depending on the temporal evolution of the flow. The treatment of finite-depth erodible bed layers, i.e. partially erodible beds, in bedload models based on the equilibrium approach has usually been made using numerical fixes, which correct the unphysical results obtained in some cases. Generally, the presence of a finite-depth erodible layer implies the introduction of a kind of non-equilibrium condition in the bedload transport state. Nevertheless, this common natural bed configuration has not been previously considered in the development of numerical models. In this work, a finite volume model (FVM) for bedload transport based on non-capacity approach and dealing with finite-depth erodible layers is proposed. New expressions for the actual bedload transport rate and the net exchange flux through the static-moving bed layers interface are used to develop a numerical scheme which solves the coupled shallow water and non-capacity bedload transport system of equations. The reconstruction of the intermediate states for the

*Corresponding author: sermar@unizar.es

local Riemann problem at each intercell edge is designed to correctly model the presence of non-erodible strata, avoiding the appearance of unphysical results in the approximate solution without reducing the time step. The new coupled scheme is tested against laboratory benchmarking experiments in order to demonstrate its stability and accuracy, pointing out the properties of both equilibrium and non-equilibrium formulations.

Keywords:
Finite volume method, shallow water equations, non-capacity bedload transport, fully coupled method, augmented Roe's scheme, finite-depth erodible layer

1. Introduction

Sediment transport is an important process which is commonly seen in natural water bodies such as rivers, dams and estuaries. The sediment particles can be transported by two basic mechanisms: suspended load which is composed by the particles moving inside the flow with the same velocity as the fluid, and bedload which involves the particles moving in a relatively thin layer over the static bed. In this bedload layer or active layer, the sediment particles remain in contact with the bed and their velocity is generally much lower than the fluid velocity [1]. Although the total load transported by suspension can be much larger than the sediment weight moving in the active bed layer [2], the bedload mechanism plays an important role and it can cause marked and rapid changes in the bed bathymetry. Relevant investigations have been carried out by means of laboratory experiments or field measurements [3–9], but they are mostly limited by the small scale of the laboratory flumes or the fact that field measurements are very time-consuming, expensive and extremely difficult to perform. Therefore, numerical modelling is an attractive tool to understand and predict the morphodynamical evolution of rivers and reservoirs. However, uncertainties arise in computational simulations due to simplifications, assumptions and empirical relationships introduced into the mathematical models used for sediment transport prediction [1]. Moreover, modelling sediment transport involves an increasing complexity with respect to static-bed shallow water models [10, 11] due to the presence of variable sediment-fluid mixture properties, coupling of physical processes and multiple layers phenomena [12].

The solid particles can be transported under equilibrium (capacity or

saturated) conditions or non-capacity (non-equilibrium or unsaturated) conditions. The classical equilibrium approach assumes that the actual sediment transport rates for suspended and bedload are equal to the capacity of the flow to carry solid weight. They are only determined by instantaneous local flow features and can be formulated by different empirical closure relations found in literature [1]. Models based on this assumption are commonly called equilibrium or capacity transport models [13–22]. On the other hand, in non-capacity models, the actual transport rates are computed through advection and mass exchange with the static erodible bed. Non-equilibrium (i.e. non-capacity) sediment transport models have been proposed [23–32] for both suspended and bedload transport. Natural morphodynamical systems such as alluvial rivers are always changing in time and space and hence absolute equilibrium states rarely exist in natural conditions. Therefore, intuitively non-capacity approaches are more suitable than models based on the equilibrium assumption since they account for the temporal and spatial delay of the actual sediment transport rate with respect to its potential capacity. However, if this adaptation delay is sufficiently small, equilibrium models can be also applied at least in theory [2].

Unlike purely suspended load models, where it has been demonstrated that the non-capacity assumption is necessary to compute correctly the solid suspended concentration and the bed evolution [29, 33], the importance of assuming non-equilibrium conditions in bedload numerical models remains uncertain. Van-Rijn [34] suggested that the actual bedload transport rate in unsteady flows can be assumed equal to the bedload capacity because the adjustment of the transported sediment particles to the new flow conditions proceeds rapidly close to the bed surface. This assumption was conceptual and without a theoretical or numerical justification. Cao et al. [29, 35] analysed numerically the multiple time scales involved in bedload transport for fluvial processes. They found that, at least for flood cases, the bedload transport rate was able to rapidly adapt to the local flow features, which justifies the widespread application of the equilibrium models [35]. However, a comparative analysis of both capacity and non-capacity bedload models in highly erosive unsteady flows, as dam-break waves or overtopping dyke-collapses, remains unperformed, especially including experimental benchmarking cases and accurate numerical schemes. This comparative analysis is the first main contribution of the present work.

The assumption of non-equilibrium conditions in a bedload mathematical model leads to the requirement of computing the temporal evolution of the

active layer thickness and the velocity of the bedload particles in order to predict the actual transport rate, as well as the net exchange flux between static and moving bed layers. This requirement introduces a high uncertainty in non-capacity models due to the calibration of the parameters associated to solid particles velocity, active layer thickness and bedload erosion-deposition rates for transient flows, which can be an annoying task with few empirical supporting data. Different strategies have been proposed in order to overcome this uncertainty. Wu [2] and El Kadi Abderrezzak et al. [36] proposed to approximate the net exchange flux through the static-moving bed layers interface by the difference between the actual and capacity transport rates affected by an adaptation length and to assume a non-storage mass condition for the active bed layer, leading to the quasi-steady solid flux relaxation models. A more complex approach was also proposed by [25, 27, 37], based on the same adaptation length parameter to determine the net exchange flux through the interface but accounting now for the mass storage in the active bed layer. This approach leads to the direct computation of the actual transport rate as one of the unknown conserved variables, assuming that the velocity in the active layer can be evaluated by one of the empirical closure relations for capacity conditions found in literature [38–40].

Recently, new and more complex approaches to the bedload non-equilibrium transport phenomenon have been derived based on a pioneering work [41]. The physical interaction between flow and sediment particles at the static-moving bed layer interface was studied at a grain scale. Zech et al. [4] modelled the net exchange flux through the interface as a function of the shear stress at the moving layer and at the upper boundary of the static layer. Fernández-Nieto et al. [30, 42] proposed new empirical formulae for the erosion and deposition rates at the interface, as well as a new closure relation for the actual sediment transport rate which reduces to the classical one under equilibrium conditions. Bohorquez and Ancey [32] also analysed erosion and deposition rates at the static-moving interface including a new diffusion term in the bedload conservation equations.

Furthermore, the presence of bedrock strata underlying the erodible alluvial layers is ubiquitous in natural rivers and estuaries. When a non-erodible layer is reached by erosion, the actual bedload transport rate over it can be affected and becomes different from the transport capacity of the flow, leading to a non-equilibrium transport state even under nearly uniform flow regimes. Some recent approaches to this topic consist on small adaptations of the classical bedload transport theory or on simple numerical fixes. Stru-

iksma [43] proposed to reduce the capacity transport rate in regions where the sediment becomes partially unavailable using a parameter based on the actual sediment thickness over the non-erodible layer and the theoretical active layer thickness for the capacity transport state. Rulot et al. [44] proposed an iterative method to correct the over-eroded cells by affecting the sediment distribution after each time step computation. Caviedes-Voullième et al. [45] implemented a numerical fix based on the limitation of the numerical solid flux at the intercell edges as a function of the available sediment volume at the involved cells. Although these simplified approaches to the finite-depth erodible layer problem seem to work reasonably well in some conditions, they offer a limited modelling ability of the real physical phenomenon and require a more detailed analysis.

In this work a new finite volume numerical scheme (FVM) is proposed, based on the non-equilibrium bedload transport assumption. A modified version of the augmented Roe Riemann solver (A-Roe) [22, 46] has been used to compute an approximate solution for the coupled system of equations (shallow water and non-capacity bedload transport) at each intercell local Riemann problem. The presence of finite-depth erodible layers is directly taken into account for the computation of the actual bedload transport rate and the reconstruction of intermediate states of the approximate solution, avoiding the unphysical negative sediment thickness appearance. Also, the proposed formulation includes the equilibrium condition as a particular case. Therefore, the numerical method developed is unique and offers identical properties for the evaluation of the relative performance of both formulations. This paper is structured as follows: in Section 2 an expression for the net exchange flux through the interface separating the static and the moving bed layers is proposed based on a grain-scale inertial analysis of the erosion-deposition phenomenon, and a new generalized Grass-type formula for the actual bedload transport rate is derived. Section 3 is devoted to the mathematical model, assuming finite sediment thickness conditions and the non-capacity bedload transport approach. In Section 4 the proposed A-Roe scheme is introduced, analysing its stability region. Also the updating procedure is reported. In Section 5 the characteristics of the approximate solution at each local RP are analysed and new reconstruction techniques, based on [47], are proposed to avoid unphysical results without affecting the stability region. Numerical results are reported in Section 6, consisting of a hypothetical case with the aim of analysing the effects of non-equilibrium formulation in the bedload transport, and several experimental benchmark-

ing tests in order to demonstrate the stability and accuracy of the proposed model. Finally, the conclusions have been drawn in Section 7. Furthermore, in Appendix A, Appendix B, Appendix C and Appendix D some extra details about the mathematical model and the numerical scheme have been provided.

2. Generalized non-capacity formulation for bedload transport

The conservation property for the sediment mass involved in bedload transport processes (Fig. 1) can be expressed by means of the 1D continuity equation for both the erodible bed layer:

$$\frac{\partial z_b}{\partial t} + \frac{\partial\, \xi q_s}{\partial x} = 0 \tag{1}$$

and the static bed layer:

$$\frac{\partial z_f}{\partial t} = \xi\,(\dot{\eta}_d - \dot{\eta}_e) \tag{2}$$

with $\xi = 1/(1-p)$, being p the bed porosity and q_s $[L^2T^{-1}]$ the actual bedload transport rate, z_b $[L]$ the bed elevation above the datum , z_f $[L]$ the static layer elevation above the datum and $(\dot{\eta}_d - \dot{\eta}_e)$ $[LT^{-1}]$ the net mass exchange flux through the interface separating the moving (active) and the static bed layers.

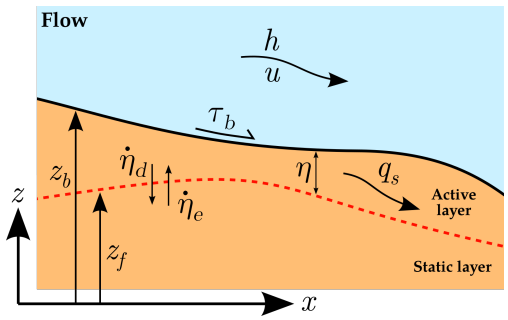

Figure 1: Bedload sediment transport sketch.

Operating (1) and (2), the mass conservation equation for the active layer can also be derived:

$$\frac{\partial \eta}{\partial t} + \frac{\partial\, \xi q_s}{\partial x} = -\xi\,(\dot{\eta}_d - \dot{\eta}_e) \tag{3}$$

where $\eta = z_b - z_f$ $[L]$ is the thickness of the active bed layer.

From a grain-scale inertial analysis [41], new closure relations for the erosion and deposition rates, $\dot{\eta}_e$ and $\dot{\eta}_d$ respectively, can be derived as:

$$\dot{\eta}_e = k_e \frac{\Delta\theta}{s} \frac{\sqrt{(s-1)g d_s^3}}{d_s} \qquad \dot{\eta}_d = k_d \frac{\eta}{d_s} \frac{\sqrt{(s-1)g d_s^3}}{d_s} \tag{4}$$

being k_e an erosion constant, k_d a deposition constant, $s = \rho_s/\rho_w$ the sediment relative density, d_s $[L]$ the median diameter of the sediment particles. The complete derivation of these expressions for the erosion and deposition rates is presented in Appendix A. The function $\Delta\theta$ involves the incipient motion criterion for the bedload transport process and is expressed as:

$$\Delta\theta = \begin{cases} \theta - \theta_c & \text{if } \theta > \theta_c \\ 0 & \text{Otherwise} \end{cases} \tag{5}$$

where $\theta = |\tau_b|/[(\rho_s - \rho_w) g d_s]$ is the non-dimensional Shields stress, θ_c is the critical value of the Shields stress for the incipient motion threshold, g $[LT^{-2}]$ is the gravity acceleration and $|\tau_b| = \rho_w g n^2 |u|^2 h^{-1/3}$ $[ML^{-1}T^{-2}]$ is the shear stress at the bed surface, being n $[TL^{-3}]$ the Manning's roughness parameter, h $[L]$ the flow depth and u $[LT^{-1}]$ the flow velocity.

Closure relations found in literature for the solid transport rate under capacity (equilibrium) conditions $\bar{q}_s$ can be written generally as:

$$\begin{aligned} |\bar{q}_s| =& c\, \theta^{m_1}\, \Delta\theta^{m_2}\, \sqrt{(s-1)g d_s^3} \\ \text{with:} \quad \theta =& \frac{n^2 |u|^2}{(s-1) d_s h^{1/3}} \end{aligned} \tag{6}$$

Formulation	c	m_1	m_2	θ_c
MPM [48]	8	0	3/2	0.047
Nielsen [49]	12	1/2	1	0.047
Fernández-Luque [50]	5.7	0	3/2	0.037
Wong [6]	3.97	0	3/2	0.0495
Smart[51]	$4 \left(\frac{d_{90}}{d_{30}}\right)^{0.2} S^{0.6} \frac{h^{1/6}}{n\sqrt{g}}$	1/2	1	0.047

Table 1: Coefficient c, m_1, m_2 and θ_c for different capacity solid transport rate formulations (6). The parameter S in the Smart formulation is the bed slope.

For all the formulations in Table 1 it can be demonstrated that $|\bar{q}_s| \propto h^{-1/2}\,|u|^3$ and hence a general formulation for the solid transport rate based on the Grass law ($|\bar{q}_s| = G|u|^3$) has been adopted by other authors [19, 20, 22]. This formulation relates the equilibrium bedload sediment discharge with the depth-averaged flow velocity by means of factor $G(h,\theta)$ $[T^2L^{-1}]$ which represents the interaction between the flow and the bed layer and which depends only on the flow characteristics. Nevertheless, when finite-depth erodible layers are involved, the sediment depth can be smaller than the theoretical thickness required to develop the capacity active layer or it can even become unavailable in some regions temporally. In these cases, the actual solid transport rate should be reduced respect to its equilibrium value (6), even under steady and uniform flow conditions. The actual transport rate depends not only on the flow features but also on the sediment availability. Hence the common formulation for the Grass interaction factor G is no longer valid. New formulations for the solid transport rate taking into account the availability of sediment have to be considered when finite-depth erodible layers are present.

Moreover, in the capacity approach the erosion and deposition rates are equal ($\dot{\eta}_d = \dot{\eta}_e$) and hence, using (4), the active layer thickness under equilibrium conditions $\bar{\eta}$ can be expressed as:

$$\bar{\eta} = \frac{k_e}{s\,k_d}\,\Delta\theta\,d_s \tag{7}$$

Note that in this case, the moving layer thickness depends only on the Shields dimensionless stress excess and the grain size. Therefore, under equilibrium conditions, (2) can be neglected and (1) reduces to the well-known Exner equation [52].

Combining the expressions for the erosion and deposition rates in (4), the following relation can be derived:

$$\eta\frac{\dot{\eta}_e}{\dot{\eta}_d} = \frac{k_e\,d_s}{s\,k_d}\,\Delta\theta \quad \rightarrow \quad \eta = \frac{\dot{\eta}_d}{\dot{\eta}_e}\,\bar{\eta} \tag{8}$$

Assuming a direct proportionality between the active layer thickness and actual solid transport rate, from (6) and (8), it is possible to derive a closure relation for the non-capacity solid transport rate:

$$|q_s| = c\,\theta^{m_1}\,\Delta\theta^{(m_2-1)}\,\frac{s\,k_d\,\eta}{k_e\,d_s}\sqrt{(s-1)g d_s^3} \tag{9}$$

Note that (9) can be rewritten as:

$$|q_s| = |u_s|\,\eta \tag{10}$$

where $|u_s|$ $[LT^{-1}]$ is the mean velocity of the bedload sediment mass in the active layer:

$$|u_s| = c\,\theta^{m_1}\,\Delta\theta^{(m_2-1)}\,\frac{s\,k_d}{k_e}\,\frac{\sqrt{(s-1)g d_s^3}}{d_s} \tag{11}$$

Rewriting (9) in the Grass law form, the sediment-fluid interaction parameter G becomes not only a function of the water depth h and the Shields parameter θ, but it also depends on the moving layer thickness η:

$$q_s = G(h,\theta,\eta)\,|u|^2 u \qquad \text{with:} \quad G = \Gamma_1(h)\,\Gamma_2(\theta)\,\Gamma_3(\eta) \tag{12}$$

As displayed in Table 2, the parameter Γ_3 is similar for all the empirical relations considered, whereas the parameters Γ_1 and Γ_2 depend on the selected formulation. This is the first of the novelties presented in the present work.

Formulation	$\Gamma_1(h)$	$\Gamma_2(\theta)$	$\Gamma_3(\eta)$	θ_c
MPM	$\frac{n^3\sqrt{g}}{(s-1)\sqrt{h}}$	$\frac{8\sqrt{\Delta\theta}}{\theta^{3/2}}$	$\frac{s\,k_d}{k_e}\frac{\eta}{d_s}$	0.047
Nielsen	$\frac{n^3\sqrt{g}}{(s-1)\sqrt{h}}$	$\frac{12}{\theta}$	$\frac{s\,k_d}{k_e}\frac{\eta}{d_s}$	0.047
Fernandez-Luque	$\frac{n^3\sqrt{g}}{(s-1)\sqrt{h}}$	$\frac{5.7\sqrt{\Delta\theta}}{\theta^{3/2}}$	$\frac{s\,k_d}{k_e}\frac{\eta}{d_s}$	0.037
Wong	$\frac{n^3\sqrt{g}}{(s-1)\sqrt{h}}$	$\frac{3.97\sqrt{\Delta\theta}}{\theta^{3/2}}$	$\frac{s\,k_d}{k_e}\frac{\eta}{d_s}$	0.0495
Smart	$\frac{n^2}{(s-1)h^{1/3}}$	$\left(\frac{d_{90}}{d_{30}}\right)^{0.2}\frac{4\,S^{0.6}}{\theta}$	$\frac{s\,k_d}{k_e}\frac{\eta}{d_s}$	0.047

Table 2: New non-capacity Grass interaction factor G for different solid transport rate formulations.

The new expression for the Grass interaction factor G takes into account the actual thickness of the moving bed layer and allows to limit the actual solid discharge $|q_s|$ when non-erodible strata are reached. Moreover, if time, flow features and sediment availability are enough to develop steady states in the bedload transport process, the erosion and deposition rates tend to be equal and the solid transport rate recovers the common closure relation (6) for equilibrium transport conditions.

In the present model, the net exchange flux through the static-moving bed layers interface can be calculated as $\dot{\eta}_d - \dot{\eta}_e$ using (4). Other authors [26, 37, 53] assumed a length L_b $[L]$ for the bedload discharge adaptation to its equilibrium state and calculated this exchange flux as $(q_s - \bar{q}_s)/L_b$ $[LT^{-1}]$, where $\bar{q}_s$ is the capacity bedload transport rate and q_s the actual transport rate. Comparison of both methods to determine the erosion-deposition net flux indicates that the proposed model assumes a dynamic value for the adaptation length L_b which is scaled following:

$$L_b \propto \frac{\sqrt{\theta}}{k_e}\, d_s \tag{13}$$

According to (13), the reduction of the erosion constant k_e leads to increasing dynamic adaptation length values and enhances non-equilibrium bedload transport states. On the other hand, the higher the Shields stress, the longer the distance that the bedload discharge needs to reach its equilibrium state and hence highly erosive flows require higher values of the adaptation length L_b. This dependency of the adaptation length with the shear stress has not been previously derived. Instead, most of the models assume a global value based on the dominant bed form [2].

As a summary, the main features of the new generalized formulation for the bedload transport are the following:

- For both capacity or non-capacity hypothesis, the bed layer continuity is modelled using (1):

$$\frac{\partial z_b}{\partial t} + \frac{\partial\, \xi q_s}{\partial x} = 0$$

- The generalized solid discharge is calculated using (12):

$$q_s = G(h, \theta, \eta)\, |u|^2 u \qquad \text{with:} \quad G = \Gamma_1(h)\, \Gamma_2(\theta)\, \Gamma_3(\eta)$$

- The assumption of non-capacity implies to calculate the temporal evolution of the active layer thickness η using (3):

$$\frac{\partial \eta}{\partial t} + \frac{\partial\, \xi q_s}{\partial x} = -\xi\, (\dot{\eta}_d - \dot{\eta}_e)$$

- Alternatively, the capacity hypothesis consists of a particular case of the generalized bedload formulation. The bedload transport rate q_s

collapses to the capacity transport rate $\bar{q}_s$ assuming an equilibrium active layer thickness $\bar{\eta}$ calculated using (7):

$$\bar{\eta} = \frac{k_e}{s\, k_d}\, \Delta\theta\, d_s$$

3. Governing equations for bedload transport with finite-depth erodible layers

The bedload transport process is controlled by the mass and momentum conservation equations for the flow and the mass conservation equations for the bed layer. The potential presence of a non-erodible layer (Fig. 2) requires to decompose the bed elevation into two parts:

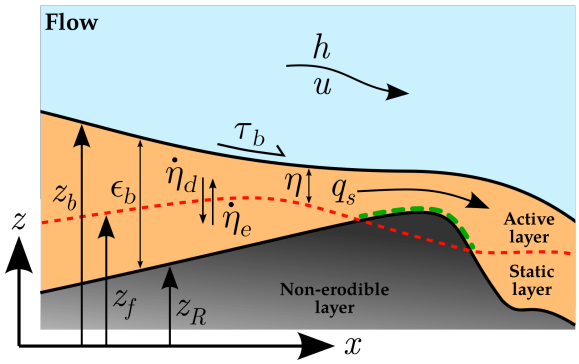

Figure 2: Bed load sediment transport sketch in presence of non-erodible layers.

$$z_b(x,t) = z_R(x) + \epsilon_b(x,t) \tag{14}$$

being $z_R(x)$ $[L]$ the non-erodible layer elevation and $\epsilon_b(x,t)$ $[L]$ the thickness of sediments over the non-erodible stratum, i.e. the depth of the finite erodible layer. It is worth stressing that this sediment layer thickness is not the same as the active layer thickness η. Then, the depth-averaged system of governing equations for a 1D flow per unit width can be written as:

$$\begin{aligned}
&\frac{\partial h}{\partial t} + \frac{\partial q}{\partial x} = 0 \\
&\frac{\partial q}{\partial t} + \frac{\partial}{\partial x}(hu^2 + \frac{1}{2}gh^2) = -gh\frac{\partial z_R}{\partial x} - gh\frac{\partial \epsilon_b}{\partial x} - ghS_f \\
&\frac{\partial \epsilon_b}{\partial t} + \frac{\partial\, \xi q_s}{\partial x} = 0
\end{aligned} \tag{15}$$

being h, $q = hu$ and ϵ_b the conserved variables, $S_f = n^2|u|uh^{-4/3}$ the friction slope caused by the shear stress on the bed layer and q_s the actual solid transport rate.

Using (12), it is possible to split the solid discharge derivative as follows:

$$\begin{aligned}\frac{\partial\, \xi q_s}{\partial x} = \frac{\partial}{\partial x}(\xi G u^3) = \xi G \frac{\partial u^3}{\partial x} + \xi u^3 \frac{\partial G}{\partial x} = \\ = \xi G \left(-ud\frac{\partial h}{\partial x} + d\frac{\partial q}{\partial x} \right) + \xi u^3 \frac{\partial G}{\partial x}\end{aligned} \tag{16}$$

being $d = 3u^2/h$. Therefore, the spatial derivative of the solid flux is divided in two terms related with the flow features variation and a third term depending on the Grass factor variation.

This allows to separate the convective flux vector as:

$$\frac{\partial \vec{F}(\vec{U})}{\partial x} = \frac{\partial \vec{F}^J(\vec{U})}{\partial x} + \frac{\partial \vec{F}^G(\vec{U})}{\partial x} \tag{17}$$

defining the Jacobian component of the convective flux $\frac{\partial \vec{F}^J(\vec{U})}{\partial x}$ as:

$$\frac{\partial \vec{F}^J(\vec{U})}{\partial x} = \begin{pmatrix} \frac{\partial q}{\partial x} \\ \frac{\partial}{\partial x}(hu^2 + \frac{1}{2}gh^2) \\ \xi G \frac{\partial u^3}{\partial x} \end{pmatrix} \tag{18}$$

and the corrector flux vector $\frac{\partial \vec{F}^G(\vec{U})}{\partial x}$:

$$\frac{\partial \vec{F}^G(\vec{U})}{\partial x} = \begin{pmatrix} 0 \\ 0 \\ \xi u^3 \frac{\partial G}{\partial x} \end{pmatrix} \tag{19}$$

Note that the flux variation term $\frac{\partial \vec{F}^G(\vec{U})}{\partial x}$ represents a corrector component for the solid flux variation in (18) and is caused by the spatial changes on the flow-sediment interaction parameter G. This corrector flux vector is mainly influenced by the presence of non-erodible layers which can reduce the value of the physical solid discharge regardless of the local flow conditions.

According to (17) and adding the non-conservative term $gh\frac{\partial \epsilon_b}{\partial x}$ to the right hand side of the momentum equation, the system (15) can be rewritten in vector form as:

$$\frac{\partial \vec{U}}{\partial t} + \mathbf{J}(\vec{U})\frac{\partial \vec{U}}{\partial x} + \mathbf{H}(\vec{U})\frac{\partial \vec{U}}{\partial x} + \frac{\partial \vec{F}^G(\vec{U})}{\partial x} = \vec{S}(\vec{U}) \tag{20}$$

with:

$$\mathbf{J}(\vec{U}) = \frac{\partial \vec{F}^J}{\partial \vec{U}} = \begin{bmatrix} 0 & 1 & 0 \\ c^2 - u^2 & 2u & 0 \\ -\xi G u d & \xi G d & 0 \end{bmatrix} \qquad \mathbf{H}(\vec{U}) = \begin{bmatrix} 0 & 0 & 0 \\ 0 & 0 & gh \\ 0 & 0 & 0 \end{bmatrix}$$

$$\vec{S}(\vec{U}) = (0, -gh\frac{\partial z_R}{\partial x} - ghS_f,\, 0)^T$$

being $\vec{U} = (h, q, \epsilon_b)^T$ the vector of conserved variables, $\mathbf{J}(\vec{U})$ the Jacobian matrix of the convective fluxes, $\mathbf{H}(\vec{U})$ the matrix of the non-conservative fluxes, $\vec{S}(\vec{U})$ the remaining source terms vector and $c = \sqrt{gh}$ the celerity of the infinitesimal waves.

Moreover, an additional equation should be considered for the temporal evolution of the active layer thickness η under non-capacity conditions:

$$\frac{\partial \eta}{\partial t} + \frac{\partial\, \xi q_s}{\partial x} = -\xi(\dot{\eta}_d - \dot{\eta}_e) \tag{21}$$

4. Numerical scheme

The system of equations (20) is solved according to a finite volume method (FVM). The numerical method proposed here for bed-load transport is based on the reconstruction, evolution and averaging steps method proposed originally by [54]. The domain is divided in computational cells of size $\Delta x = x_{i+\frac{1}{2}} - x_{i-\frac{1}{2}}$ and a piecewise constant representation of the exact solution $\vec{U}$ is assumed. The theory of Riemann problems can be applied to the intercell discontinuities. Even when the exact solution of the RP is unknown, it is possible to estimate its variation by integrating (21) over a suitable control volume. Moreover, to compute the solution evolution, Godunov methods allow the use of linearized approximate or weak solutions for the local RP at the intercell edges.

Therefore, assuming known piecewise constant values of $\vec{U}$ for the i-cell at the time t^n, the first order Godunov's method provides updated cell averaged values for the conserved variables at the next time t^{n+1} using the following explicit expression:

$$\vec{U}_i^{n+1} = \vec{U}_i^n - \frac{\Delta t}{\Delta x}\left(\vec{F}^{*-}_{i+\frac{1}{2}} - \vec{F}^{*+}_{i-\frac{1}{2}}\right) \tag{22}$$

where Δt is the time step and $\vec{F}^{*\mp}_{i\pm\frac{1}{2}}$ represents the numerical flux at the intercell edges. The numerical flux contains all the information regarding convective Jacobian fluxes, corrector solid flux and source terms and will be formulated using an upwind scheme derived from the original augmented Roe's scheme (ARoe) proposed by [46].

The proposed ARoe scheme for bedload transport solves an approximate linear RP of constant coefficients associated to the edge $i+\frac{1}{2}$, expressed as:

$$\begin{aligned} &\frac{\partial \widehat{U}}{\partial t} + \widetilde{\mathbf{M}}_{i+\frac{1}{2}} \frac{\partial \widehat{U}}{\partial x} + \frac{\partial \widetilde{F}^{G}_{i+\frac{1}{2}}}{\partial x} = \widetilde{S}_{i+\frac{1}{2}} \\ &\widehat{U}(x,0) = \begin{cases} U_i & \text{if } x < 0 \\ U_{i+1} & \text{if } x > 0 \end{cases} \end{aligned} \tag{23}$$

being $U_i = \vec{U}^n_i$, $U_{i+1} = \vec{U}^n_{i+1}$ and $\widehat{U}(x,t)$ the approximate solution. The approximate Jacobian matrix and corrector flux vector, and the integrated source terms vector depend on the values of the conserved variables at the left and right cells, that is $\widetilde{\mathbf{M}}_{i+\frac{1}{2}} = \widetilde{\mathbf{M}}(U_i, U_{i+1})$, $\widetilde{F}^{G}_{i+\frac{1}{2}} = \widetilde{F}^{G}(U_i, U_{i+1})$ and $\widetilde{S}_{i+\frac{1}{2}} = \widetilde{S}(U_i, U_{i+1})$.

The constant coefficient matrix $\widetilde{\mathbf{M}}_{i+\frac{1}{2}}$ for the linearized RP at the intercell edge is defined as:

$$\widetilde{\mathbf{M}}_{i+\frac{1}{2}} = \widetilde{\mathbf{J}}(U_i, U_{i+1}) + \widetilde{\mathbf{H}}(U_i, U_{i+1}) = \begin{bmatrix} 0 & 1 & 0 \\ \widetilde{c}^2 - \widetilde{u}^2 & 2\widetilde{u} & \widetilde{c}^2 \\ -\xi \widetilde{G} \widetilde{u} \widetilde{d} & \xi \widetilde{G} \widetilde{d} & 0 \end{bmatrix} \tag{24}$$

Integrating both the exact non-conservative system (20) and the linearized system (23) over a suitable control volume, and imposing the consistency condition for the approximated solution $\widehat{U}(x, t^n)$:

$$\int_{-\Delta x/2}^{\Delta x/2} \vec{U}(x,t^n)dx = \int_{-\Delta x/2}^{\Delta x/2} \widehat{U}(x,t^n)dx \tag{25}$$

leads to:

$$\Delta t \int_{-\Delta x/2}^{\Delta x/2} \left(\frac{\partial \vec{F}^J}{\partial x} + \mathbf{H} \frac{\partial \vec{U}}{\partial x} \right) dx + \Delta t \int_{-\Delta x/2}^{\Delta x/2} \frac{\partial \vec{F}^G}{\partial x} dx - \int_{-\Delta x/2}^{\Delta x/2} \int_{t^n}^{t^{n+1}} \vec{S}\, dt\, dx =$$

$$= \Delta t \left(\widetilde{\mathbf{M}} \delta U + \delta \widetilde{F}^G \right)_{i+\frac{1}{2}} - \int_{-\Delta x/2}^{\Delta x/2} \int_{t^n}^{t^{n+1}} \widetilde{S}_{i+\frac{1}{2}}\, dt\, dx \tag{26}$$

From (26), the following conditions have been derived for the linearized Jacobian matrix $\widetilde{\mathbf{M}}_{i+\frac{1}{2}}$ and corrector flux vector $\widetilde{F}^G_{i+\frac{1}{2}}$:

$$\begin{aligned} &\int_{-\Delta x/2}^{\Delta x/2} \left(\frac{\partial \vec{F}^J}{\partial x} + \mathbf{H} \frac{\partial \vec{U}}{\partial x} \right) dx = \delta \widetilde{F}^M_{i+\frac{1}{2}} = \widetilde{\mathbf{M}}_{i+\frac{1}{2}} \delta U_{i+\frac{1}{2}} \\ &\int_{-\Delta x/2}^{\Delta x/2} \frac{\partial \vec{F}^G}{\partial x} dx = \delta \widetilde{F}^G_{i+\frac{1}{2}} = \left(0,\, 0,\, \xi \widetilde{u}^3\, \delta G\right)^T_{i+\frac{1}{2}} \end{aligned} \tag{27}$$

being $\delta \widetilde{F}^M_{i+\frac{1}{2}}$ the part of the convective fluxes that is modelled by means of the approximate Jacobian matrix $\widetilde{\mathbf{M}}$ at the interface edge. The source terms have been integrated assuming the following time linearization:

$$\int_{-\Delta x/2}^{\Delta x/2} \int_{t^n}^{t^{n+1}} \vec{S}\, dt\, dx \approx \Delta t \int_{-\Delta x/2}^{\Delta x/2} \vec{S}(U_i, U_{i+1}, t^n)\, dx \approx$$

$$\approx \Delta t \int_{-\Delta x/2}^{\Delta x/2} \widetilde{S}_{i+\frac{1}{2}}\, dx = \Delta t\, \widetilde{\mathbf{S}}_{i+\frac{1}{2}} = \Delta t \begin{pmatrix} 0 \\ -g\bar{h}\, \delta z_R - g\bar{h} \widetilde{S}_f\, \delta x \\ 0 \end{pmatrix}_{i+\frac{1}{2}} \tag{28}$$

being $\bar{h} = (h_i + h_{i+1})/2$, $\widetilde{S}_f = \bar{n}|\widetilde{u}|\widetilde{u}/\bar{h}^{4/3}$, $\bar{n} = (n_i + n_{i+1})/2$ and $\delta x = x_{i+1} - x_i$.

Therefore, following (27) the derivation of the edge-averaged $\widetilde{c}$, $\widetilde{u}$, $\widetilde{d}$ and $\widetilde{G}$ has been done imposing:

$$\begin{cases} \delta\widetilde{F}^{M}_{i+\frac{1}{2}} = \widetilde{\mathbf{M}}(U_i, U_{i+1})\ \delta U_{i+\frac{1}{2}} \\ \widetilde{\mathbf{M}}(U_i, U_i) = \mathbf{M}(U_i) \end{cases} \tag{29}$$

with:

$$\delta\widetilde{F}^{M}_{i+\frac{1}{2}} = \begin{pmatrix} \delta q \\ \delta(hu^2 + \frac{1}{2}gh^2) + g\bar{h}\,\delta\epsilon_b \\ \xi\widetilde{G}\,\delta u^3 \end{pmatrix}_{i+\frac{1}{2}}$$

and using (16), an additional condition is also imposed to ensure the solid mass conservation property:

$$\delta(\xi q_s)_{i+\frac{1}{2}} = \xi\widetilde{G}\,\delta u^3_{i+\frac{1}{2}} + \xi\widetilde{u}^3\,\delta G_{i+\frac{1}{2}} \tag{30}$$

According to (29) and (30), the following explicit expressions can be obtained for the edge-averaged quantities $\widetilde{c}$, $\widetilde{u}$, $\widetilde{d}$:

$$\begin{aligned} \widetilde{c} &= \sqrt{g\bar{h}} \qquad \widetilde{u} = \frac{u_i\sqrt{h_i} + u_{i+1}\sqrt{h_{i+1}}}{\sqrt{h_i} + \sqrt{h_{i+1}}} \\ \widetilde{d} &= \frac{(u_i^2 + u_{i+1}^2 + u_i u_{i+1})(\sqrt{h_i} + \sqrt{h_{i+1}})}{\sqrt{h_i}h_{i+1} + h_i\sqrt{h_{i+1}}} \end{aligned} \tag{31}$$

and for the edge-averaged Grass factor $\widetilde{G}$:

$$\begin{aligned} \widetilde{G} = &\frac{(G_i h_{i+1}^{3/2} + G_{i+1}h_i^{3/2})}{(\sqrt{h_i} + \sqrt{h_{i+1}})^3} + \\ &+ \frac{3(\sqrt{h_i}h_{i+1} + h_i\sqrt{h_{i+1}})(G_i u_i^2 + G_{i+1}u_{i+1}^2) + 3u_i u_{i+1}(G_i\sqrt{h_i}h_{i+1} + G_{i+1}h_i\sqrt{h_{i+1}})}{(\sqrt{h_i} + \sqrt{h_{i+1}})^3\,(u_i^2 + u_{i+1}^2 + u_i u_{i+1})} \end{aligned} \tag{32}$$

This edge-averaged flow-sediment interaction factor $\widetilde{G}$ depends not only on the values of the Grass parameter at the left and right cells of the edge but also on the local flow features at both cells. Hence, it follows the eigenstructure of the Roe's matrix $\widetilde{\mathbf{M}}_{i+\frac{1}{2}}$ and its properties for some especial numerical situations have been analized in Appendix B.

The linearized matrix $\widetilde{\mathbf{M}}_{i+\frac{1}{2}}$ is assumed diagonalizable, with 3 different approximate real eigenvalues $\widetilde{\lambda}_1 < \widetilde{\lambda}_2 < \widetilde{\lambda}_3$ which must be computed from

the characteristic polynomial using the *Cardano-Vieta* formula [22]. Explicit expressions for the calculation of the eigenvalues of the linearized matrix have been provided in Appendix C. It is worth stressing that one eigenvalue is always opposite to the velocity direction and two of them have the same sign.

$$\begin{cases} \widetilde{\lambda}_1 < 0 < \widetilde{\lambda}_2 < \widetilde{\lambda}_3 & \text{if } \widetilde{u} > 0 \\ \widetilde{\lambda}_1 < \widetilde{\lambda}_2 < 0 < \widetilde{\lambda}_3 & \text{if } \widetilde{u} < 0 \end{cases} \tag{33}$$

Therefore, $\widetilde{\mathbf{M}}_{i+\frac{1}{2}}$ can be expressed as:

$$\widetilde{\mathbf{M}}_{i+\frac{1}{2}} = (\widetilde{\mathbf{P}}\widetilde{\mathbf{\Lambda}}\widetilde{\mathbf{P}}^{-1})_{i+\frac{1}{2}} \qquad \text{with:} \quad \widetilde{\mathbf{\Lambda}}_{i+\frac{1}{2}} = \begin{bmatrix} \widetilde{\lambda}_1 & 0 & 0 \\ 0 & \widetilde{\lambda}_2 & 0 \\ 0 & 0 & \widetilde{\lambda}_3 \end{bmatrix} \tag{34}$$

where matrix $\widetilde{\mathbf{P}}_{i+\frac{1}{2}}$ is constructed as $\widetilde{\mathbf{P}} = (\vec{\widetilde{e}}_1, \vec{\widetilde{e}}_2, \vec{\widetilde{e}}_3)$, being $\vec{\widetilde{e}}_m$ the eigenvector associated to the eigenvalue $\widetilde{\lambda}_m$ and obtained imposing the condition $\widetilde{\mathbf{M}}_{i+\frac{1}{2}}\vec{\widetilde{e}}_m = \widetilde{\lambda}_m\vec{\widetilde{e}}_m$:

$$\vec{\widetilde{e}}_m = \left(1,\, \widetilde{\lambda}_m,\, \frac{(\widetilde{\lambda}_m - \widetilde{u})^2 - \widetilde{c}^2}{\widetilde{c}^2}\right)^T_{i+\frac{1}{2}} \tag{35}$$

Following [55], the conserved variable differences $\delta U_{i+\frac{1}{2}}$ and source term spatial integral $\widetilde{\mathbf{S}}_{i+\frac{1}{2}}$ at the intercell edge are projected on the eigenvector basis in order to obtain the wave and source strength vectors, $\widetilde{A}_{i+\frac{1}{2}}$ and $\widetilde{B}_{i+\frac{1}{2}}$ respectively.

$$\begin{aligned} \widetilde{A}_{i+\frac{1}{2}} &= (\widetilde{\alpha}_1,\, \widetilde{\alpha}_2,\, \widetilde{\alpha}_3)^T = (\widetilde{\mathbf{P}}^{-\mathbf{1}}\delta U)_{i+\frac{1}{2}} \quad \longrightarrow \quad \delta U_{i+\frac{1}{2}} = \sum_m \widetilde{\alpha}_m \vec{\widetilde{e}}_m \\ \widetilde{B}_{i+\frac{1}{2}} &= (\widetilde{\beta}_1,\, \widetilde{\beta}_2,\, \widetilde{\beta}_3)^T = (\widetilde{\mathbf{P}}^{-\mathbf{1}}\widetilde{\mathbf{S}})_{i+\frac{1}{2}} \quad \longrightarrow \quad \widetilde{\mathbf{S}}_{i+\frac{1}{2}} = \sum_m \widetilde{\beta}_m \vec{\widetilde{e}}_m \end{aligned} \tag{36}$$

A complete description of the explicit expressions obtained for the wave and source strengths can be found in Appendix C.

Furthermore, the corrector flux vector (27) can be split as $\delta\widetilde{F}^G_{i+\frac{1}{2}} = \delta\widetilde{F}^{G-}_{i+\frac{1}{2}} + \delta\widetilde{F}^{G+}_{i+\frac{1}{2}}$, defining:

$$\delta\widetilde{F}^{G-}_{i+\frac{1}{2}} = \begin{pmatrix} 0 \\ 0 \\ \xi\widetilde{u}^3\,\delta G^- \end{pmatrix}_{i+\frac{1}{2}} \qquad \delta\widetilde{F}^{G+}_{i+\frac{1}{2}} = \begin{pmatrix} 0 \\ 0 \\ \xi\widetilde{u}^3\,\delta G^+ \end{pmatrix}_{i+\frac{1}{2}} \tag{37}$$

being $\delta G^-_{i+\frac{1}{2}} = \widetilde{G} - G_i$ and $\delta G^+_{i+\frac{1}{2}} = G_{i+1} - \widetilde{G}$. This splitting of the corrector vector is directly controlled by the value of the Grass interaction parameter $\widetilde{G}$ at the intercell edge an hence it is directly linked to the Jacobian matrix eigenstructure. The corrector flux at the left cell $\delta\widetilde{F}^{G-}_{i+\frac{1}{2}}$ can be associated to the fastest wave traveling with negative velocity, whereas the corrector flux at the right cell $\delta\widetilde{F}^{G+}_{i+\frac{1}{2}}$ can be associated to the fastest wave travelling with positive velocity. The Rankine-Hugoniot conditions for the split corrector fluxes lead to:

$$\begin{aligned} \delta\widetilde{F}^{G-}_{i+\frac{1}{2}} &= \widetilde{\lambda}_1\,\delta U^{G-}_{i+\frac{1}{2}} \\ \delta\widetilde{F}^{G+}_{i+\frac{1}{2}} &= \widetilde{\lambda}_3\,\delta U^{G+}_{i+\frac{1}{2}} \end{aligned} \tag{38}$$

being $\delta U^{G-}_{i+\frac{1}{2}}$ and $\delta U^{G+}_{i+\frac{1}{2}}$ the intermediate solution variation associated to the corrector fluxes. The second novelty of the present work is this upwind splitting of the convective solid flux associated to the Grass factor variation between cells. An explanation about the necessity of including this corrector flux to ensure the solid mass conservation in the local RP has been included in Appendix D.

One consequence of Roe's linearization is that the resulting approximate solution of the local RP at the incercell edge is reconstructed using only discontinuities and $\vec{U}(x,t)$ consists of a sum of jumps or shocks. The construction of the upwind numerical fluxes required in (22) is based on the properties of the linearized Jacobian matrix eigenstructure [47]. According to Godunov's method, it is sufficient to provide the solution for $\vec{U}(x,t)$ at the intercell edge position $x = x_{i+\frac{1}{2}}$ in order to obtain the associated numerical fluxes.

The reconstruction of the approximate solution at the left and right side of the intercell edge, U_i^- and U_{i+1}^+ respectively, can be expressed as:

$$
\begin{aligned}
U_i^- &= U_i + \left(\sum_{m-} \widetilde{\gamma}_m \vec{\widetilde{e}}_m\right)_{i+\frac{1}{2}} + \delta U_{i+\frac{1}{2}}^{G-} \\
U_{i+1}^+ &= U_{i+1} - \left(\sum_{m+} \widetilde{\gamma}_m \vec{\widetilde{e}}_m\right)_{i+\frac{1}{2}} - \delta U_{i+\frac{1}{2}}^{G+}
\end{aligned}
\tag{39}
$$

where $\widetilde{\gamma}_m = \widetilde{\alpha}_m - \widetilde{\beta}_m/\widetilde{\lambda}_m$ and the subscript index $m-$ and $m+$ under the sums indicate waves traveling with negative and positive velocities, respectively.

Therefore, the intermediate numerical fluxes at the left and right side of the intercell edge, $\vec{F}_{i+\frac{1}{2}}^{*-}$ and $\vec{F}_{i+\frac{1}{2}}^{*+}$ respectively, can be expressed as:

$$
\begin{aligned}
\vec{F}_{i+\frac{1}{2}}^{*-} \equiv \vec{F}_i^- &= \vec{F}_i + \left(\sum_{m-} \widetilde{\lambda}_m^- \widetilde{\gamma}_m \vec{\widetilde{e}}_m\right)_{i+\frac{1}{2}} + \delta \widetilde{F}_{i+\frac{1}{2}}^{G-} \\
\vec{F}_{i+\frac{1}{2}}^{*+} \equiv \vec{F}_{i+1}^+ &= \vec{F}_{i+1} - \left(\sum_{m+} \widetilde{\lambda}_m^+ \widetilde{\gamma}_m \vec{\widetilde{e}}_m\right)_{i+\frac{1}{2}} - \delta \widetilde{F}_{i+\frac{1}{2}}^{G+}
\end{aligned}
\tag{40}
$$

Finally, the first order Godunov's updating formulation (22) can be rewritten for the cell i as:

$$
\vec{U}_i^{n+1} = \vec{U}_i^n - \frac{\Delta t}{\Delta x}\left(\vec{F}_i^- - \vec{F}_i^+\right) \tag{41}
$$

Also it is possible to rewrite (41) in fluctuation form as:

$$
\vec{U}_i^{n+1} = \vec{U}_i^n - \frac{\Delta t}{\Delta x}\left(\delta \vec{F}_{i+\frac{1}{2}}^- + \delta \vec{F}_{i-\frac{1}{2}}^+\right) \tag{42}
$$

with:

$$
\delta \vec{F}_{i+\frac{1}{2}}^- = \left(\sum_{m-} \widetilde{\lambda}_m^- \widetilde{\gamma}_m \vec{\widetilde{e}}_m\right)_{i+\frac{1}{2}} + \delta \widetilde{F}_{i+\frac{1}{2}}^{G-} \qquad \delta \vec{F}_{i-\frac{1}{2}}^+ = \left(\sum_{m+} \widetilde{\lambda}_m^+ \widetilde{\gamma}_m \vec{\widetilde{e}}_m\right)_{i-\frac{1}{2}} + \delta \widetilde{F}_{i+\frac{1}{2}}^{G+} \tag{43}
$$

Therefore, the approximate solution of $\vec{U}(x,t)$ for the linearized RP at the intercell edge $i+\frac{1}{2}$ consists of 5 regions connected by 4 waves: the three waves corresponding to the linearized matrix eigenvalues $\widetilde{\lambda}_m$ plus one additional steady wave with null celerity accounting for the source terms

(Fig. 3). Considering a positive average velocity $\widetilde{u} > 0$ and using (39), the intermediate states for the conserved variables can be expressed as:

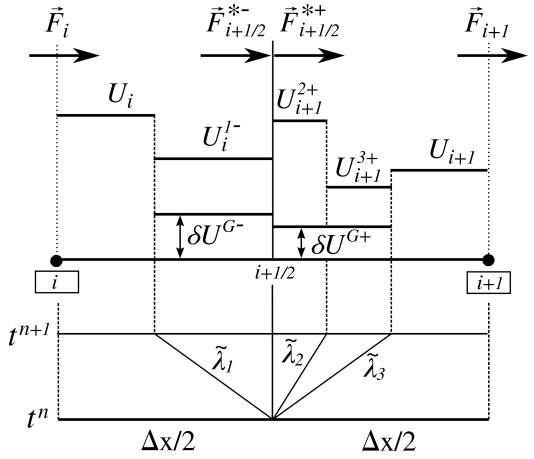

Figure 3: Approximate solution structure for the local RP at the intercell edge $i + \frac{1}{2}$.

$$
\begin{aligned}
U_i^{1-} &= U_i + \widetilde{\gamma}_1 \vec{\widetilde{e}}_1 + \delta U^{G-} \\
U_{i+1}^{2+} &= U_{i+1}^{3+} - \widetilde{\gamma}_2 \vec{\widetilde{e}}_2 \\
U_{i+1}^{3+} &= U_{i+1} - \widetilde{\gamma}_3 \vec{\widetilde{e}}_3 - \delta U^{G+}
\end{aligned}
\tag{44}
$$

so that, using (40), the associated fluxes for each intermediate state are:

$$
\begin{aligned}
\vec{F}_i^{1-} &= \vec{F}_i + \widetilde{\lambda}_1 \widetilde{\gamma}_1 \vec{\widetilde{e}}_1 + \delta \widetilde{F}^{G-} \\
\vec{F}_{i+1}^{2+} &= \vec{F}_{i+1}^{3+} - \widetilde{\lambda}_2 \widetilde{\gamma}_2 \vec{\widetilde{e}}_2 \\
\vec{F}_{i+1}^{3+} &= \vec{F}_{i+1} - \widetilde{\lambda}_3 \widetilde{\gamma}_3 \vec{\widetilde{e}}_3 - \delta \widetilde{F}^{G+}
\end{aligned}
\tag{45}
$$

For the sake of clarity, the subscript index $i + \frac{1}{2}$ has been omitted in (44) and (45). The reconstruction of the approximate solution should be analysed in order to ensure positivity of the water depth values [46]. Furthermore, the unphysical over-erosion when finite-depth erodible layers are presented has to be avoided, that is, the positivity of the sediment layer thickness has to be ensured. A detailed explanation of the approximate solution reconstruction method proposed in this work is reported in Section 5.

4.1. Resolution method with capacity and non-capacity approaches

Starting from known values of the conserved variables $(h,\, q,\, \epsilon_b)_i^n$ in the cell i at the time t^n, and the value of the active layer thickness at the same time η_i^n, applying (41) or (42) allows us to update the solution of the conserved variables to the next time t^{n+1}, i.e. $(h,\, q,\, \epsilon_b)_i^{n+1}$, regardless of the capacity or non-capacity approach has been considered. However, the updating procedure for active layer thickness depends on the assumption made for the bedload transport.

Using the capacity formulation (7), the active layer thickness at the next time step t^{n+1} is directly computed as:

$$\eta_i^{n+1} = \frac{k_e}{s\, k_d} \left(\Delta\theta\right)_i^{n+1} d_s \tag{46}$$

where $\left(\Delta\theta\right)_i^{n+1}$ is the non-dimensional Shields excess (5) at the cell i computed with the conserved variables updated to time $n+1$:

$$\left(\Delta\theta\right)_i^{n+1} = \begin{cases} \theta_i^{n+1} - \theta_c & \text{if } \theta_i^{n+1} > \theta_c \\ 0 & \text{Otherwise} \end{cases} \tag{47}$$

However, the assumption of the non-equilibrium approach leads to the necessity of solving equation (21) for each time step. In order to update the solution of the active layer thickness (η_i^{n+1}), a semi-implicit procedure is used in the present work:

1. An intermediate state is predicted using only the convective fluxes:

$$\eta_i^{n+1/2} = \eta_i^n - \frac{\Delta t}{\Delta x}\left(\vec{F}_{3,i}^{-} - \vec{F}_{3,i}^{+}\right) \tag{48}$$

   being $\vec{F}_{3,i}^{\pm}$ the numerical solid fluxes at the intercell edge (40).

2. Intermediate values of the erosion and deposition rates, $\dot{\eta}_{e,i}^{n+1/2}$ and $\dot{\eta}_{d,i}^{n+1/2}$ respectively, are computed using:

$$\begin{aligned} \dot{\eta}_{e,i}^{n+1/2} &= k_e \frac{\left(\Delta\theta\right)_i^{n+1}}{s} \frac{\sqrt{(s-1)g d_s^3}}{d_s} \\ \dot{\eta}_{d,i}^{n+1/2} &= k_d \frac{\eta_i^{n+1/2}}{d_s} \frac{\sqrt{(s-1)g d_s^3}}{d_s} \end{aligned} \tag{49}$$

3. The value of η is finally updated to the next time t^{n+1} incorporating the net exchange flux at the static-moving bed layers interface:

$$\eta_i^{n+1} = \eta_i^{n+1/2} - \Delta t\, \xi\, (\dot{\eta}_{d,i}^{n+1/2} - \dot{\eta}_{ei}^{n+1/2}) \tag{50}$$

Independently of capacity or non-capacity assumption, once the active layer thickness has been updated, its value has to be limited in presence of non-erodible layers:

$$\text{If } \eta_i^{n+1} > \epsilon_{bi}^{n+1} \quad \rightarrow \quad \eta_i^{n+1} = \epsilon_{bi}^{n+1} \tag{51}$$

and the actual solid rate for the next time step $n+1$ is computed as:

$$q_{s,i}^{n+1} = G_i^{n+1} \left(|u_i^{n+1}|\right)^2 u_i^{n+1} \tag{52}$$

with:

$$G_i^{n+1} = \Gamma_1(h_i^{n+1})\ \Gamma_2(\theta_i^{n+1})\ \Gamma_3(\eta_i^{n+1}) \tag{53}$$

This mechanism effectively reduces the actual solid transport rate q_s in cells which are close to be fully scoured by the flow and hence it improves the stability of the proposed scheme in regions where finite-depth erodible layers exist.

4.2. Stability region

The time step should be dynamically limited to ensure that there is no interaction of waves from neighboring Riemann problems. If the positivity of the water depth h and the erodible layer thickness ϵ_b values at the intermediate states of the solution is guaranteed, in order to construct an updated cell average solution $\vec{U}_i^{n+1}$, it is only necessary that the average values at the intercell edges remain constant in time over the entire time step. This unique requirement allows us to define an upper limit for the time step depending only on the characteristic waves celerity and the spatial cell size. In consequence, the stability region at the intercell edge $i+\frac{1}{2}$ is defined as:

$$\Delta t^{\tilde{\lambda}}|_{i+\frac{1}{2}} = \frac{\Delta x}{\max\limits_m(|\widetilde{\lambda}_m|)_{i+\frac{1}{2}}} \tag{54}$$

Therefore, the global time step for the updated solution calculation is obtained applying a CFL condition:

$$\Delta t = \text{CFL} \min_{i=1}^{N-1}(\Delta t^{\tilde{\lambda}}|_{i+\frac{1}{2}}) \tag{55}$$

where CFL ≤ 1 and N is the total number of cells in which the conserved variables should be solved at each time calculation.

5. Approximate solution reconstruction and positivity control with finite-depth erodible layers

5.1. Active control of the sediment thickness positivity (AC-STP)

This is a common issue in sediment transport numerical schemes dealing with finite-depth sediment layers [12, 30, 43–45, 56], which requires to control the numerical solution in order to ensure non-negative values of the sediment mass, i.e. avoiding over-eroded cells where sediment mass is numerically created leading to accuracy, conservation and stability issues. A widely extended strategy [43, 45, 56] to deal with this drawback is to reduce the time step, ensuring in this way the positivity of the cell averaged ϵ_b^{n+1} values but leading to an important increase of the computational effort. On the other hand, in the context of SW equations over static bed, [46] proposed for the water depth variable h a new reconstruction strategy based on enforcing positivity on the intermediate solutions of the linearized RP at the intercell edge. The method offers a twofold benefit, it avoids unphysical negative values of the cell averaged water depth and the time step is preserved. This approach is adapted in this work to SW equations involving erodible bed, where the number of waves is increased, focusing on the active control of the sediment thickness ϵ_b positivity (AC-STP). This reconstruction procedure for the approximate solution is the third main novelty presented in this work.

Considering $\widetilde{u} > 0$ and (44), the solution at the next time ϵ_b^{n+1} at the left cell (Fig. 4) can be evaluated as:

$$\begin{aligned} &\epsilon_{bi}^{n+1} = \epsilon_{bi}^{n} + \frac{|\widetilde{\lambda}_1|\Delta t}{\Delta x/2}(\epsilon_{bi}^{1-} - \epsilon_{bi}^{n}) \geq 0 \\ &\text{with:} \quad \epsilon_{bi}^{1-} = \epsilon_{bi}^{n} + \widetilde{\gamma}_1 \widetilde{e}_1^3 + \delta\epsilon_b^{G-} \end{aligned} \tag{56}$$

being ϵ_{bi}^{1-} the sediment thickness intermediate state associated to the wave 1 and $\delta\epsilon_b^{G-}$ the sediment thickness jump due to the variation of the Grass

factor between cell-center i and cell-edge $i+\frac{1}{2}$ (38). For the right cell it can be expressed as:

$$\epsilon_{bi+1}^{n+1} = \epsilon_{bi+1}^{n} + \frac{\widetilde{\lambda}_2 \Delta t}{\Delta x/2}(\epsilon_{bi+1}^{2+} - \epsilon_{bi+1}^{3+}) + \frac{\widetilde{\lambda}_3 \Delta t}{\Delta x/2}(\epsilon_{bi+1}^{3+} - \epsilon_{bi+1}^{n}) \geq 0$$
$$\text{with:} \quad \begin{cases} \epsilon_{bi+1}^{2+} = \epsilon_{bi+1}^{3+} - \widetilde{\gamma}_2 \widetilde{e}_2^3 \\ \epsilon_{bi+1}^{3+} = \epsilon_{bi+1}^{n} - \widetilde{\gamma}_3 \widetilde{e}_3^3 - \delta\epsilon_b^{G+} \end{cases} \tag{57}$$

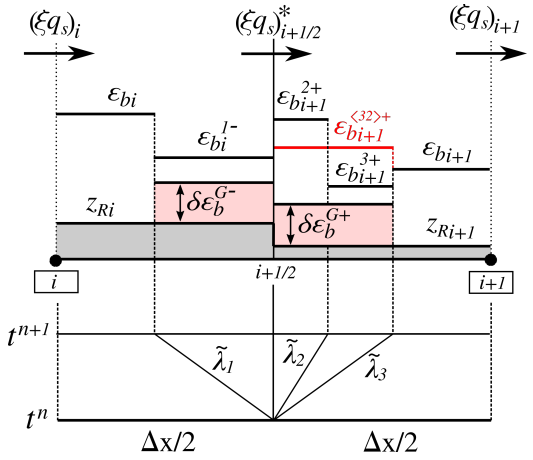

Figure 4: Intermediate states for the erodible layer thickness ϵ_b at the intercell edge $i+\frac{1}{2}$.

being ϵ_{bi+1}^{2+}, ϵ_{bi+1}^{3+} the sediment thickness intermediate states associated to the waves 2 and 3 and $\delta\epsilon_b^{G+}$ the sediment thickness jump due to the variation of the Grass factor between cell-edge $i+\frac{1}{2}$ and cell-center $i+1$ (38). The right cell approximate solution in (57) can be rewritten defining an averaged intermediate sediment thickness $\epsilon_{bi+1}^{\langle 32\rangle +}$ at the right side of the edge:

$$\epsilon_{bi+1}^{\langle 32\rangle +} = \epsilon_{bi+1}^{3+} - \frac{\widetilde{\lambda}_2}{\widetilde{\lambda}_3}\widetilde{\gamma}_2 \widetilde{e}_2^3 \tag{58}$$

Introducing (58) in (57), the right sediment thickness average solution can be rewritten in the following way:

$$\epsilon_{bi+1}^{n+1} = \epsilon_{bi+1}^{n} + \frac{\widetilde{\lambda}_3 \Delta t}{\Delta x/2}(\epsilon_{bi+1}^{\langle 32\rangle +} - \epsilon_{bi+1}^{n}) \geq 0 \tag{59}$$

The stability condition requires both $\frac{|\widetilde{\lambda}_1|\Delta t}{\Delta x/2} \leq 1$ and $\frac{\widetilde{\lambda}_3\Delta t}{\Delta x/2} \leq 1$. Hence, from (56) and (59), we can derive the conditions $\epsilon_{bi}^{1-} \geq 0$ and $\epsilon_{bi+1}^{\langle 32\rangle+} \geq 0$ respectively to ensure positive cell averaged solutions.

Since the presence of a finite-depth erodible layer and its influence in the solid intercell flux is mainly contained in the corrector flux vector, the following limits for the corrector sediment thickness jump are proposed:

$$\begin{aligned} \delta\epsilon_b^{G-} &\geq (\delta\epsilon_b^{G-})^{MIN} = -(\epsilon_{bi}^n + \widetilde{\gamma}_1\widetilde{e}_1^3) \\ \delta\epsilon_b^{G+} &\leq (\delta\epsilon_b^{G+})^{MAX} = \epsilon_{bi+1}^n - \frac{\widetilde{\lambda}_2}{\widetilde{\lambda}_3}\widetilde{\gamma}_2\widetilde{e}_2^3 - \widetilde{\gamma}_3\widetilde{e}_3^3 \end{aligned} \tag{60}$$

and the following strategy is suggested:

a) If $\epsilon_{bi}^{1-} < 0$ and $\epsilon_{bi+1}^{\langle 32\rangle+} > 0$

1. $\delta\epsilon_b^{G-} = (\delta\epsilon_b^{G-})^{MIN}$
2. $\delta\widetilde{F}^{G-} = \begin{pmatrix} 0 \\ 0 \\ \widetilde{\lambda}_1\,\delta\epsilon_b^{G-} \end{pmatrix} \qquad \delta\widetilde{F}^{G+} = \delta\widetilde{F}^G_{i+\frac{1}{2}} - \delta\widetilde{F}^{G-}$ (61)
3. $\delta\epsilon_b^{G+} = \delta\widetilde{F}^{G+}/\widetilde{\lambda}_3$
4. If $\delta\epsilon_b^{G+} > (\delta\epsilon_b^{G+})^{MAX}$, reduce Δt until (59) becomes true.

b) If $\epsilon_{bi}^{1-} > 0$ and $\epsilon_{bi+1}^{\langle 32\rangle+} < 0$

1. $\delta\epsilon_b^{G+} = (\delta\epsilon_b^{G+})^{MAX}$
2. $\delta\widetilde{F}^{G+} = \begin{pmatrix} 0 \\ 0 \\ \widetilde{\lambda}_3\,\delta\epsilon_b^{G+} \end{pmatrix} \qquad \delta\widetilde{F}^{G-} = \delta\widetilde{F}^G_{i+\frac{1}{2}} - \delta\widetilde{F}^{G+}$ (62)
3. $\delta\epsilon_b^{G-} = \delta\widetilde{F}^{G-}/\widetilde{\lambda}_1$
4. If $\delta\epsilon_b^{G-} < (\delta\epsilon_b^{G-})^{MIN}$, reduce Δt until (56) becomes true.

Since the solid discharge q_s, and hence the Grass parameter G, have already been reduced at cells by limiting the actual moving layer thickness η when a non-erodible stratum is reached, the step 4 of the above strategy is a guarantee for extreme cases.

5.2. *Wet/Dry treatment for sediment fronts*

A special situation can occur when a sediment front arrives to a non-erodible step higher than the erodible bed elevation (Fig. 5). In a discrete approach, considering a positive velocity $\widetilde{u} > 0$ at the edge $i+\frac{1}{2}$, the direction of the numerical solid flux at the intercell edge $(\xi q_s)^*_{i+\frac{1}{2}}$ is also positive and hence the sediment mass is transfered from cell i to cell $i+1$. But if the bed level at the left cell $(z_{Ri} + \epsilon_{bi})$ is lower than the non-erodible stratum elevation at the right cell (z_{Ri+1}), the solid mass transfer can suffer of a physical obstacle that is not considered in the numerical scheme. If the non-erodible step is high enough, the sediment mass transfer between cells is canceled by means of a nil numerical solid flux at the intercell edge.

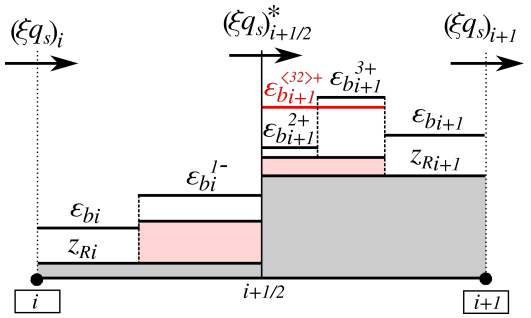

Figure 5: Approximate states for the erodible layer thickness ϵ_b at the intercell edge $i+\frac{1}{2}$, considering the presence of a non-erodible step.

To model this physical situation, the following strategy is adopted in the present work if $(z_R + \epsilon_b)_i < z_{Ri+1}$ and $(\xi q_s)^*_{i+\frac{1}{2}} > 0$:

a) If $(z_R + \epsilon_b^{1-})_i > z_{Ri+1}$ the sediment progresses normally and the numerical solid flux $(\xi q_s)^*_{i+\frac{1}{2}}$ is computed as in (40).

b) If $(z_R + \epsilon_b^{1-})_i \leq z_{Ri+1}$ the sediment can not progress to the cell $i+1$

and hence $(\xi q_s)^*_{i+\frac{1}{2}}$ is set null applying the following strategy:.

1. $\delta\epsilon_b^{G-} = \dfrac{(\xi q_s)_i + \widetilde{\lambda}_1\widetilde{\gamma}_1\widetilde{e}_1^3}{|\widetilde{\lambda}_1|}$
2. $\delta\widetilde{F}^{G-} = \begin{pmatrix} 0 \\ 0 \\ \widetilde{\lambda}_1\,\delta\epsilon_b^{G-} \end{pmatrix} \qquad \delta\widetilde{F}^{G+} = \delta\widetilde{F}^{G}_{i+\frac{1}{2}} - \delta\widetilde{F}^{G-}$ (63)
3. $\delta\epsilon_b^{G+} = \delta\widetilde{F}^{G+}/\widetilde{\lambda}_3$
4. If $\delta\epsilon_b^{G+} > (\delta\epsilon_b^{G+})^{MAX}$, reduce Δt until (59) becomes true.

This technique allows the correct treatment of the advance of sediment front over steeped non-erodible layers, also ensuring the solid mass conservation and avoiding marked time step reductions.

6. Numerical tests

6.1. Transport of a finite-depth rectangular dune

The aim of this original test case is to study the influence of the non-capacity assumption on the transport of a non-cohesive rectangular dune over a non-erodible layer with positive slope. A domain $100\,m$ long ($\Delta x = 1\,m$) is considered with a non-erodible layer constant slope of $0.1\,\%$. The rectangular dune is placed at $20\,m < x < 40\,m$ and its initial thickness is set to $1\,m$. A constant inlet water discharge of $q_{in} = 5m^2/s$ is considered and the water depth at the outlet is set to $h_{out} = 1.99\,m$. The Manning's roughness coefficient is $n = 0.02\,sm^{-1/3}$ for both the sediment material and the non-erodible layer. The sediment features are: density $\rho_s = 2650\,kg/m^3$, particle diameter $d_s = 1\,mm$, internal friction angle $\phi_e = 35°$, porosity $p = 0.4$. The effects of both the deposition constant value and the relation between erosion and deposition constants will be analized in detail using this erosive numerical test.

The initial state for the sediment transport simulation was calculated developing the flow for static-bed conditions until steady state was reached (Fig. 6). The initial flow regime was subcritical in the whole domain except at $39\,m < x < 40\,m$, where a supercritical regime was reached. To compute the bed-load solid transport rate the proposed Meyer-Peter-Müller formulation (see Table 2) was chosen. The deposition constant was initially set to $k_e = 0.3$ with a relation $k_e/k_d = 10$ according to literature values [32, 42].

Also the initial value for active layer thickness η was set to its value under equilibrium state $\bar{\eta}$ using (7).

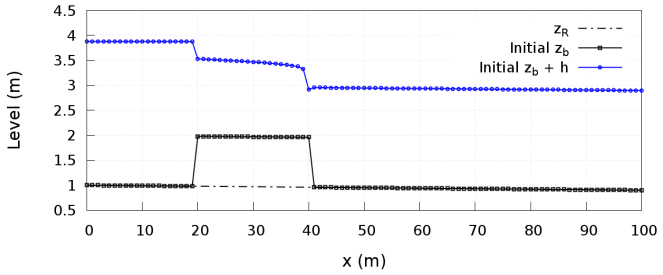

Figure 6: Initial bed and free surface level for the erosive simulations in test 6.1.

The temporal bed level evolution has been depicted in Fig. 7 considering capacity and non-capacity approaches. A visual comparison of the bed profiles at different time steps shows the most marked differences between both approaches at the tail of the dune, where the Shield stress excess $\Delta\theta$ had the highest initial values and hence the adaptation length was longer. As time progressed and the dune moved downstream, the erosion and deposition rates are high enough to allow a fast transition to equilibrium transport conditions on the bedload layer and hence the capacity and non-capacity solutions tended to approximate.

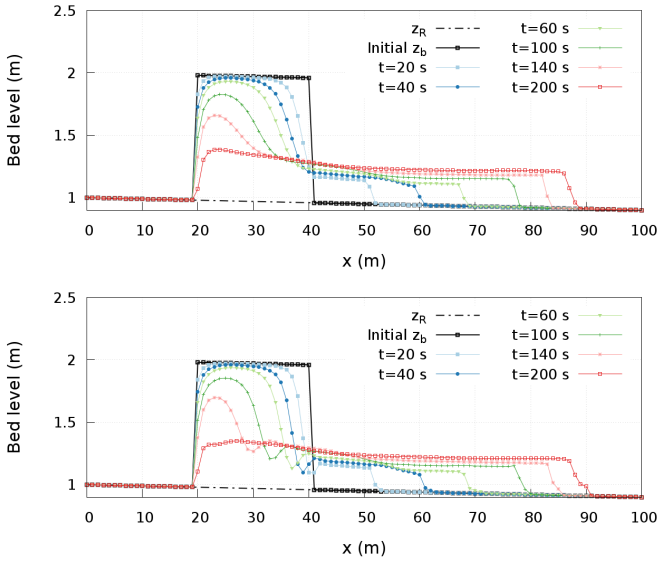

Figure 7: Bed level evolution with $k_e = 0.3$ and $k_e/k_d = 10$: (top) capacity approach and (bottom) non-capacity approach.

Calibration of the erosion and deposition rates, i.e. the net exchange flux through the static-moving bed layers interface, is a key point in non-capacity bed-load models and it has a huge influence on the numerical results. A wide range of values for the erosion and deposition constants can be found in literature [30, 32, 41, 57], leading to high uncertainty in the numerical results obtained with non-capacity models. Usually, values for the erosion constant are of the order $k_e \sim \mathcal{O}(10^{-2}, 10^{1})$, whereas the relation k_e/k_d varies from 2 to 30. Fig. 8 shows the bed level profile at different times considering non-capacity approach and k_e increasing from 0.3 to 1.0 ($k_d/k_e = 10$). Reduction of the erosion constant k_e led to an increment of the equivalent bedload adaptation length (13) and hence the transport rate differs more from the equilibrium value at the dune downward slope. This non-equilibrium state reduced the solid transport rate at the head of the downward slope and increased the transport rates at the toe with respect to the corresponding capacity transport rates. This fact caused a high erosion effect downstream the bed dune, where the flow regime changes from subcritical to supercritical, even with the same relation k_e/k_d.

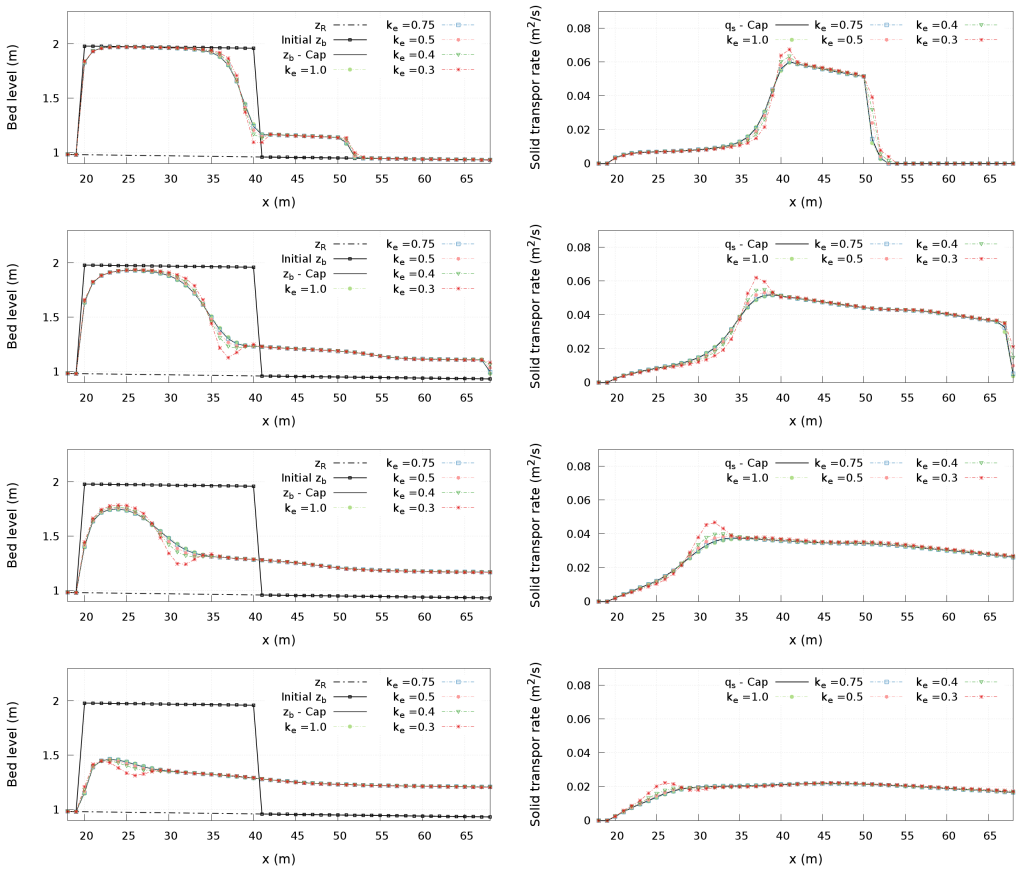

Figure 8: Influence of the deposition constant k_e value: (left) bed level and (right) solid transport rate at time (first row) $t_1 = 20\,s$, (second row) $t_2 = 60\,s$, (third row) $t_3 = 120\,s$ and (fourth row) $t_4 = 180\,s$.

Comparison of the erosion-deposition net exchange flux (see Fig. 9 - right column) along the dune domain shows the highest non-equilibrium zones at the upward and downward slopes of the rectangular dune for the first stages of the bed movement. Negative values of $\dot{\eta}_d - \dot{\eta}_e$ imply erosion of the static layer taking place whereas positive values lead to aggradation of static bed layer. An important erosive net flux appears at the downward slope of the dune associated to a strong shear-stress change (the flow is changing from subcritical to supercritical regime) and to lower values of the moving layer thickness (see Fig. 9 - left column).

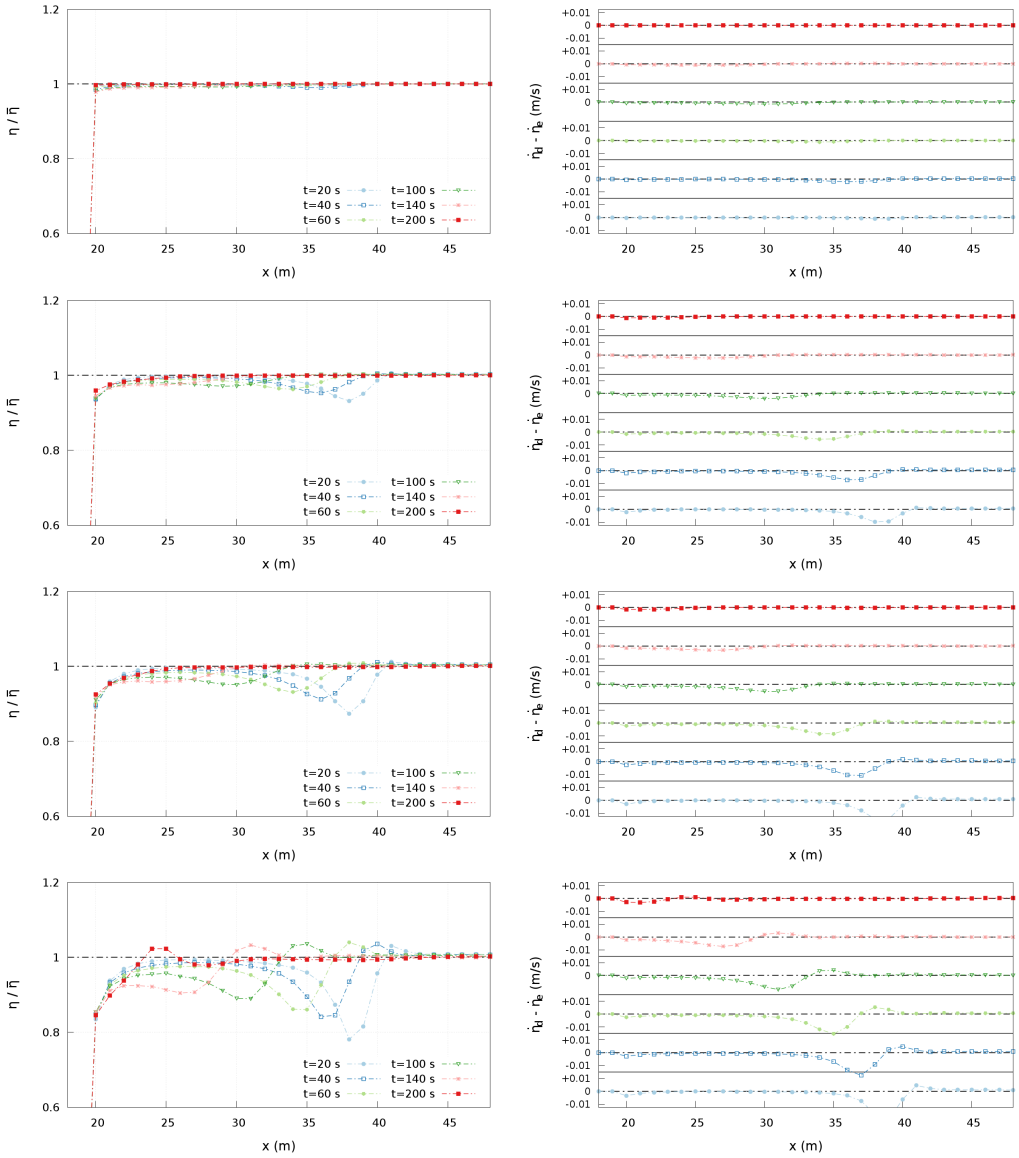

Figure 9: Influence of the deposition constant k_e value: (left) relative moving layer thickness $\eta/\bar{\eta}$ and (right) net exchange flux through the static-moving layers interface with (first row) $k_e = 0.75$, (second row) $k_e = 0.5$, (third row) $k_e = 0.4$ and (fourth row) $k_e = 0.3$.

Furthermore, two important points should be noted: first, as the bed movement progresses with time, the imbalance between erosion and deposi-

tion rates tends to disappear, which is in agreement with the non-equilibrium assumption. Second, as the erosion constant k_e decreases, the imbalance between erosion and deposition rates at the downward slope of the dune tends to become more marked and to extend in time, demonstrating an agreement between the erosion-deposition formulation proposed in this work and the classical approach for the net exchange flux adopted by other authors [2, 58].

Finally, Fig. 10 depicts the active layer thickness η computed with the non-capacity formulation at different times along the dune profile. It is worth noting that the reduction of the relation k_e/k_d led to a reduction of the moving layer thickness. However, as k_e/k_d decreased, the non-equilibrium in the bedload transport state did not show marked modifications.

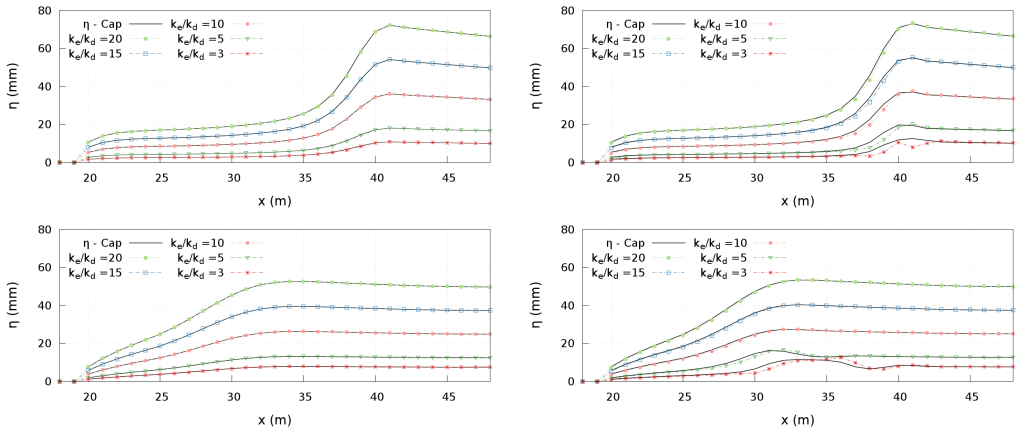

Figure 10: Influence of the erosion-deposition constants relation k_e/k_d: (first row) $t_1 = 20\,s$ and (second row) $t_2 = 120\,s$ with (left column) $k_e = 0.75$ and (right column) $k_e = 0.4$.

6.2. Dam-break over light-weight sediment flat bed

The aim of this benckmak test is to analyze the behavior of the proposed model against highly erosive unsteady flows. This experimental test [3] consists of an idealized dam-break flow over a light-weight sediment flat bed made of cylindrical PVC pellets, with equivalent diameter $d_s = 3.9\,mm$, density $\rho = 1580\,kg/m^3$, internal friction angle $\phi = 30°$ and porosity $p = 0.42$. The experiment was carried out in a 6 m long and 0.25 m width. The flume was uniformly filled to a height of 0.1 m over the flume floor with the light-weight sediment. Breaking of the dam was reproduced by the downward movement of a pneumatically actuated thin gate placed at the middle of

the flume. The initial water level was 0.35 m upstream the gate and nil downstream. Once the gate was open and the dam-break wave progressed downstream, an intense sediment transport process started instantaneously caused by the high fluid velocity and the low sediment density. The temporal evolutions of the free water surface, bed surface and static-moving bed layer interface were reported experimentally until 1.5 sec after the gate opening each 0.25 sec. The simulations have been performed with a cell size $\Delta x = 0.01\,m$, Manning roughness coefficient $n = 0.028\,s/m^3$, deposition constant $k_d = 0.03$, erosion constant $k_e = 0.2$ and CFL = 0.95. The actual transport rate has been estimated using a modified version of the MPM model with the coefficient $c = 16$ in order to correctly capture the influence of the low density of the erodible layer particles [4].

Fig. 11 shows the numerical results for the temporal evolution of the free water surface, bed level and static-moving bed layers interface with the equilibrium approach (left column) and the non-capacity approach (right column). In general, a good agreement with measured data can be found with both assumptions, especially at times greater than $t = 0.50\,sec$. For the first stages after the gate opening ($0\,s < t \leq 0.75\,s$) both models underestimate the thickness of the moving bed layer η (see Table 3 and Fig. 12). This discrepancy can be generated by the marked vertical velocities that appear at the first instants of the fluid movement [5] that can not be captured by the depth-averaged model. However, the free water surface and the bed level were well predicted (Table 3) and the propagation velocity of the dam-break wave was accurately captured (see Fig. 11). Some differences between numerical results and observed data appeared at the gate region. This region is the most affected by vertical fluid velocities at the first stages of the dam-break flow and suffers an intense erosion process during the whole experiment. It is worth mentioning that the non-equilibrium formulation was not able to improve the agreement of the computed static-moving interface level z_f and bed level z_b with those observed experimentally, compared with the results obtained using the capacity formulation. Nevertheless, the prediction of the free water surface level (WSL) computed with the non-capacity bedload transport formulation showed lower deviations respect to the experimental data than the capacity results for all the dam-break stages.

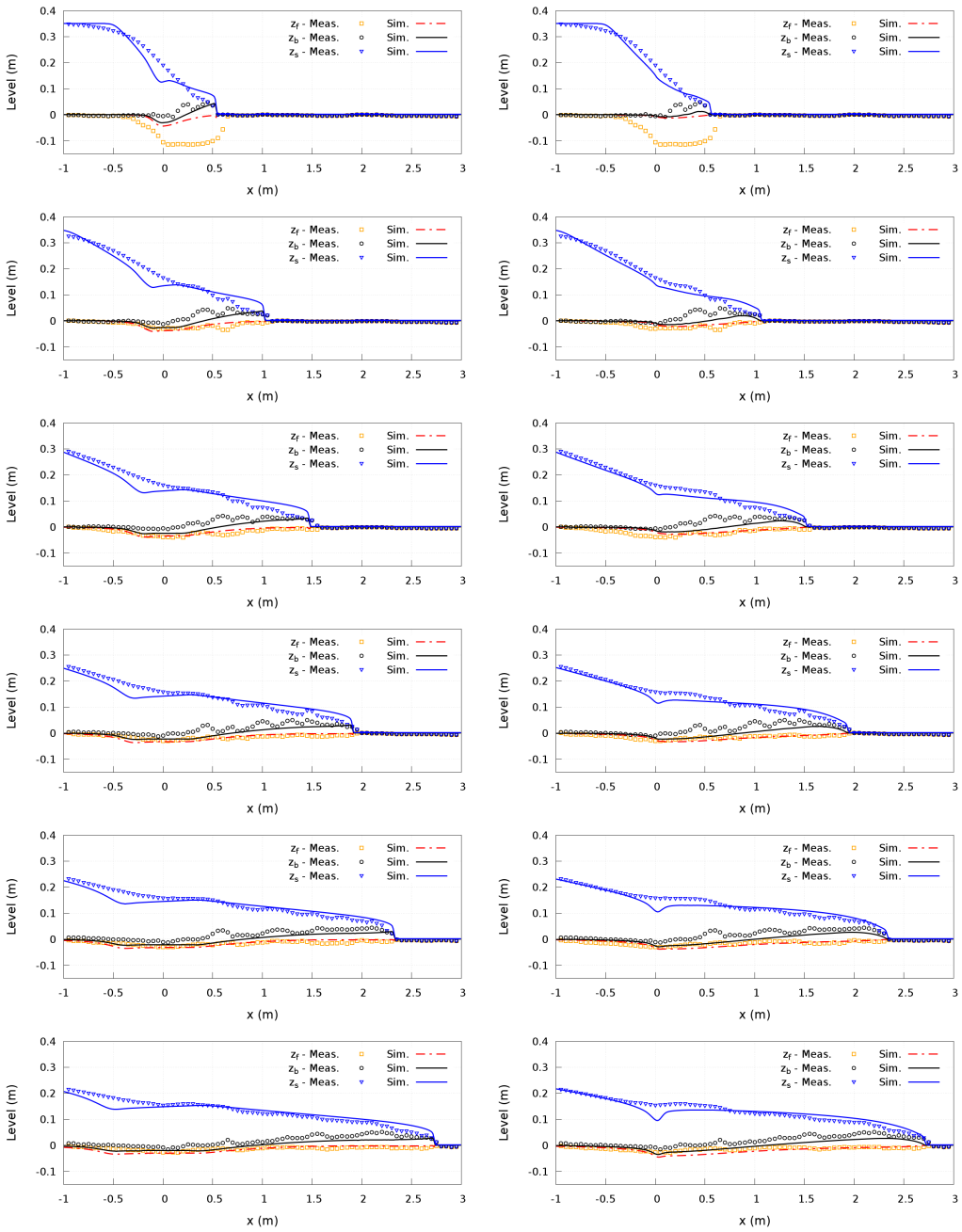

Figure 11: Free water surface, bed level and static-moving bed layers interface for (left column) equilibrium approach and (right column) non-capacity approach at times $t = 0.25\,s, 0.5\,s, 0.75\,s, 1.0\,s, 1.25\,s, 1.5\,s$ after the gate opening.

Formulation	RMSE			
	$z_f\,(m)$	$z_b\,(m)$	$WSL\,(m)$	$\eta\,(m)$
Early stages: $0\,s < t \leq 0.75\,s$				
Cap.	0.01668	0.01276	0.02032	0.02594
Non-Cap.	0.01961	0.01363	0.01472	0.02957
Later stages: $0.75\,s < t \leq 1.5\,s$				
Cap.	0.00776	0.01689	0.01819	0.01692
Non-Cap.	0.00792	0.01782	0.01623	0.01469

Table 3: RMSE for the static bed layer elevation z_f, bed level z_b, water surface level (WSL) and active bed layer thickness η with capacity and non-capacity formulations.

Fig. 12 shows the moving bed layer thickness distribution at three different times during the dam-break wave propagation. Both approaches underestimated η but the results can be considered reasonable, specially for the later stages (Table 3). For the first stages, the sediment thickness computed using the equilibrium model offer a better approximation to those observed in laboratory than the result obtained with non-capacity model. However, as time progresses and the fluid moves downstream, the non-capacity model predicts better the active thickness distribution, with lower RMSE for times larger than 0.75 s.

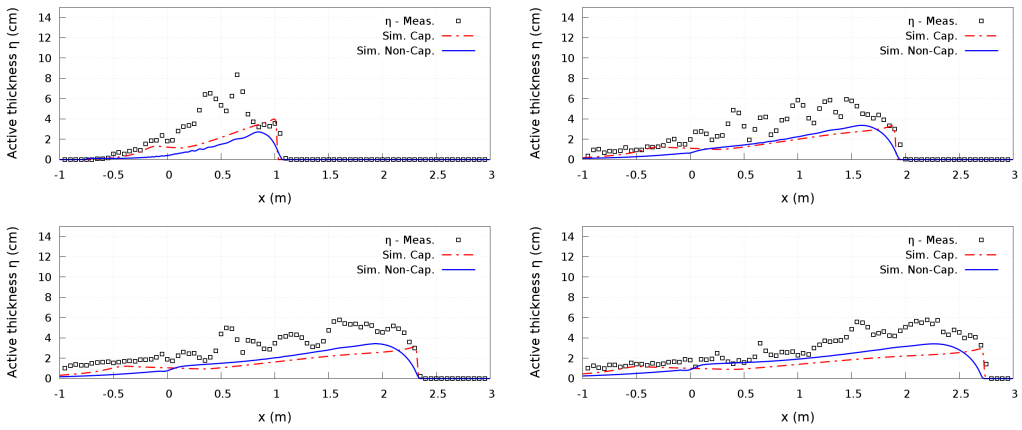

Figure 12: Moving bed layer thickness η with both equilibrium and non-capacity approaches at times (top left) $t = 0.5\,s$, (top right) $t = 1.0\,s$, (bottom left) $t = 1.25\,s$ and (bottom right) $t = 1.5\,s$.

The net exchange flux $\dot{\eta}_d - \dot{\eta}_e$ through the static-moving bed layers interface shows a marked erosive non-equilibrium for the firsts stages of the wave advance ($0 < t \leq 0.75\,s$) at the whole dam-break wave domain (see Fig. 13-top). Nevertheless, as the flow moves downstream, this net exchange flux tends to reduce generally, approaching progressively to the equilibrium state at $t = 1.5\,s$, i.e. null net exchange flux, except at the dam-break wave front and the gate region, where flow changes from subcritical to supercritical conditions. In these two regions marked erosive net exchange fluxes are maintained through the static-moving bed layers interface during the whole simulation time.

Note that in the region between the gate and the wave front, a quasi-uniform net exchange flux appears for the later stages ($0.75\,s < t \leq 1.5\,s$). In this region, the relationship between the dimensionless active layer thickness $\eta\, d_s^{-1}$ and the excess of Shields stress $\Delta\theta$ also tends progressively to quasi-uniform values as the dam-break flow progresses (see Fig. 13-bottom), i.e. $\eta\, d_s^{-1}/\Delta\theta \approx const$. It is worth mentioning that the equilibrium state is a particular case where, from (7), the relation $\bar{\eta}\, d_s^{-1}/\Delta\theta = const = k_e/(s\, k_d)$ can be derived.

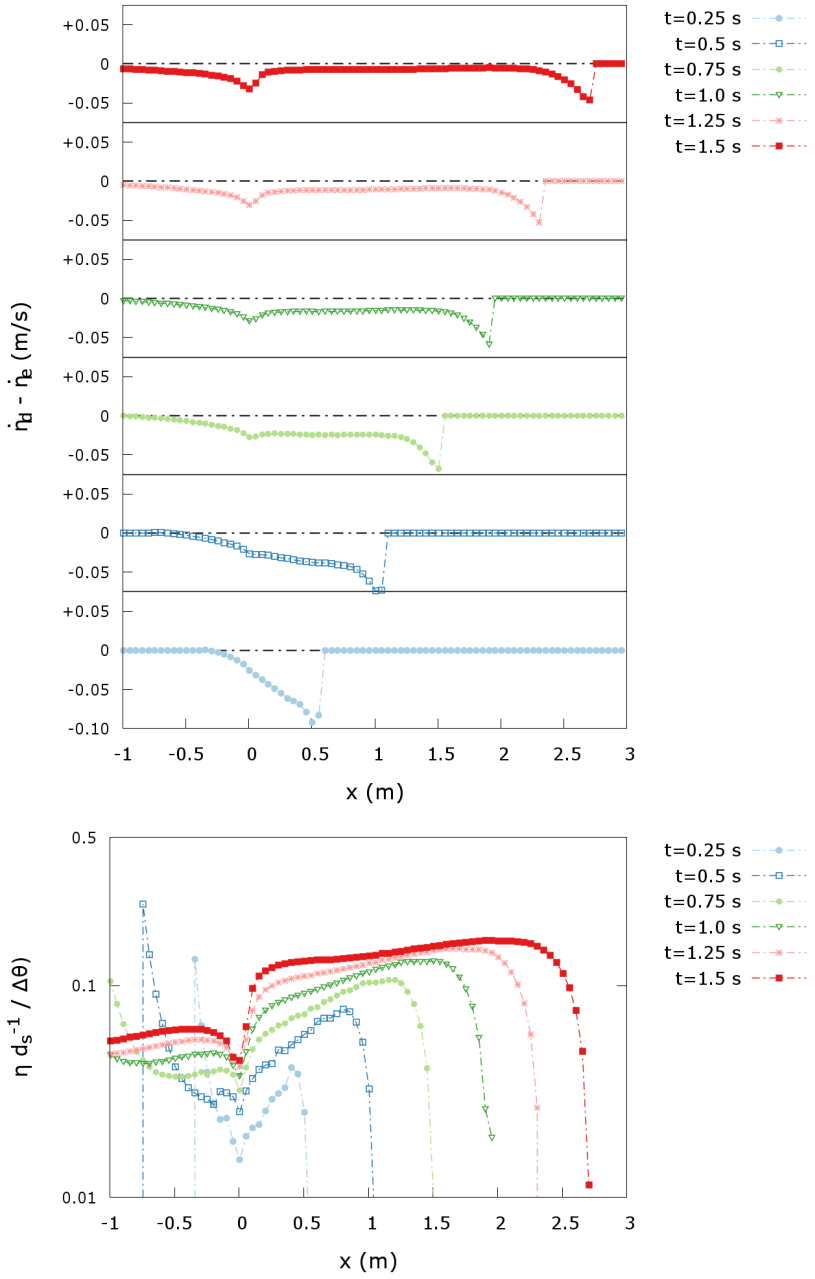

Figure 13: (Top) Net exchange flux through the static-moving bed layers interface and (bottom) relationship between the dimensionless active layer thickness $\eta\, d_s^{-1}$ and the excess of Shields stress $\Delta\theta$ at times $t = 0.25\,s, 0.5\,s, 0.75\,s, 1.0\,s, 1.25\,s, 1.5\,s$ for test 6.2.

6.3. Dike-breaking by overtopping

As in the previous case, the aim of this benchmark test is to analyze the behavior of the proposed model against highly erosive unsteady flows. This experimental test case was carried out [13] in a straight rectangular cross-section flume $35\,m$ long and $1m$ wide. A trapezoidal dyke was constructed in the middle of the flume with a non-cohesive sand of characteristic diameter $d_s = 1.13\,mm$ ($d_{30} = 0.52\,mm$, $d_{50} = 0.86\,mm$, $d_{90} = 3.80\,mm$), density $\rho = 2650\,kg/m^3$, internal stability angle $\phi = 30°$ and porosity $p = 0.22$. The height over the non-erodible flume bed and crest width of the dyke were 0.80 m and 0.30 m, respectively. A vertical plate was placed at the middle of the crest in order to achieve horizontal water surface elevations upstream the dyke. In a first step, a constant discharge was set at the flume inlet and the upstream reach was filled to a height of 3 cm over the dyke crest. Then, the plate was suddenly lifted up to allow overflow to start, maintaining the constant inlet discharge. The dyke surface evolution was recorded by photography. Temporal bed elevation data are provided at $P1 = 15\,cm$, $P2 = 65\,cm$ and $P3 = 115\,cm$ with distances measured from the midpoint of the dyke crest. The temporal evolution of the discharge at the dyke crest and the upstream reservoir level were also reported. Two different experiment, C1 and C2, have been used to test the proposed model capabilities. The inlet discharge and the dyke upstream and downstream slopes, S_u and S_d respectively, have been summarized in Table 4. The cell size for the simulations was $\Delta x = 0.01m$, the Manning's roughness coefficient was calibrated as $n = 0.15sm^{-1/3}$ and the CFL was set to 0.95. The erosion and deposition constants, k_e and k_d respectively, used in simulations for each benchmarking test have also been reported in Table 4.

Case	$q\,inlet\,(l/s)$	S_u	S_d	k_e	k_d
C1	1.05	1V:3H	1V:5H	0.4	0.02
C2	1.23	1V:3H	1V:3H	0.3	0.01

Table 4: Geometrical features and erosion-deposition constants used in the simulations for each benchmarking case in test 6.4.

6.3.1. Case C1

Fig. 14 shows the numerical results, considering the equilibrium transport assumption, for the temporal evolutions of both the reservoir level and

the discharge at the dyke crest with different empirical formulations for the bedload transport rate. Measured data have also been plotted for comparison. The Smart-CBFS formulation [59] offers the best results, especially for the discharge at the dyke crest, but overestimates the erosion of the dyke at the first stages after the overflow starting. On the other hand, both Meyer-Peter-Müller and Fernández-Luque closure relations underestimate the bedload transport rate, resulting in a slower evolution of the dyke surface and leading to a lower peak in the discharge hydrograph.

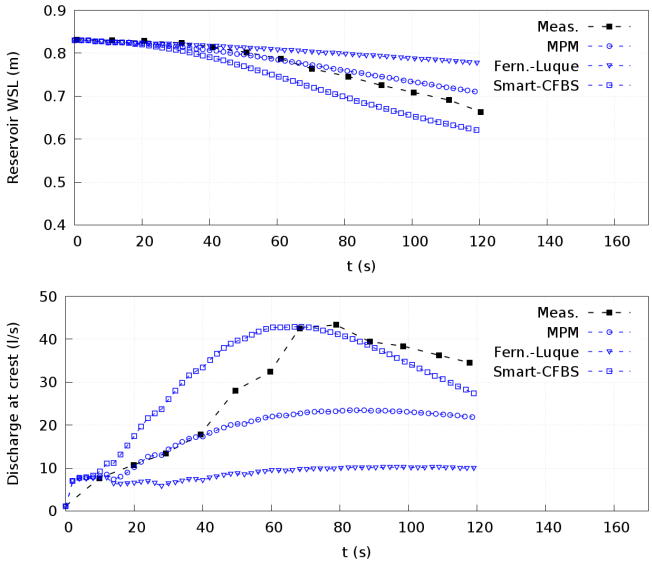

Figure 14: Temporal evolution of the (top) reservoir water surface level and (bottom) discharge at the dyke crest for the case C1: measured data compared to numerical results with equilibrium approach.

The Smart-CBFS closure relation has been chosen to study the influence of the non-capacity approach on the computed dyke surface evolution for case C1. Fig. 15 shows the numerical results considering both capacity and non-capacity approaches for the temporal evolutions of the reservoir water level and discharge at the crest. The obtained results have also been plotted against the measured data and the numerical results reported in [20], where a 2D weakly-coupled equilibrium model was used for simulations. Although the predicted peak in the discharge with non-capacity formulation is lower than those observed in the laboratory, in general the numerical results agree better with the measured data than those obtained with both the proposed

1D model under equilibrium hypothesis and the 2D model reported by [20], improving the reservoir level and discharge predictions (Table 5).

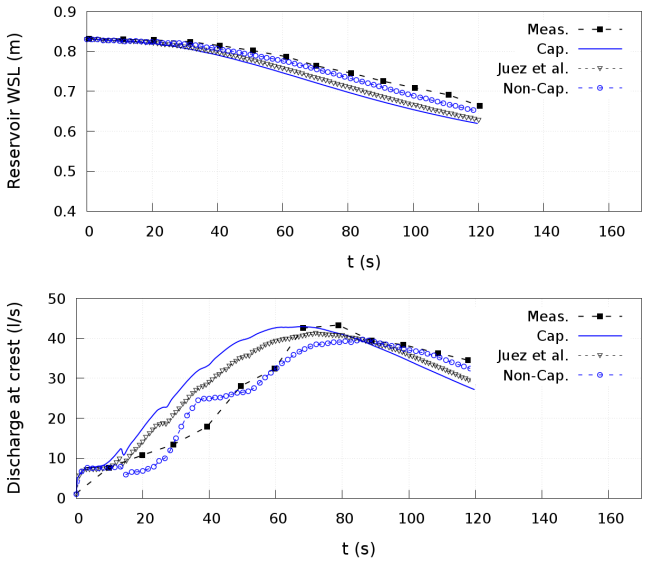

Figure 15: Temporal evolution of the (top) reservoir water surface level and (bottom) discharge at the dyke crest for the case C1 under non-capacity with modified Smart-CBFS formula.

	RMSE		
Variable	Capacity	Non-Capacity	Juez et al.
WSL_{reserv} (m)	0.03865	0.01279	0.02967
Q_{crest} (m^3/s)	0.00755	0.00304	0.00499
z_{b1} (m)	0.04191	0.02543	0.03437
z_{b2} (m)	0.03573	0.01370	0.03275
z_{b3} (m)	0.01998	0.01583	0.01959

Table 5: RMSE (case C1) for the reservoir level WSL_{reserv}, discharge at the dam crest Q_{crest}, and bed level at the probes P1 z_{b1}, P2 z_{b2} and P3 z_{b3}, with capacity and non-capacity formulations. Also RMSE for the results obtained with the Juez et al. model [20] has been reported.

685 Furthermore, the dyke bed surface evolution has been plotted in Fig. 16 at probes P1, P2 and P3, considering the modified Smart-CBFS formulation

under capacity and non capacity conditions. The non-equilibrium hypothesis is able to improve the agreement with bed evolution measured data at all the probes (see Table 5). At the first stages after the overflow starts, marked non-
690 equilibrium states are obtained by the active layer thickness η. Nevertheless, as time progresses, the bedload transport tends to reach the equilibrium state and the active layer thickness approximates its value under capacity conditions.

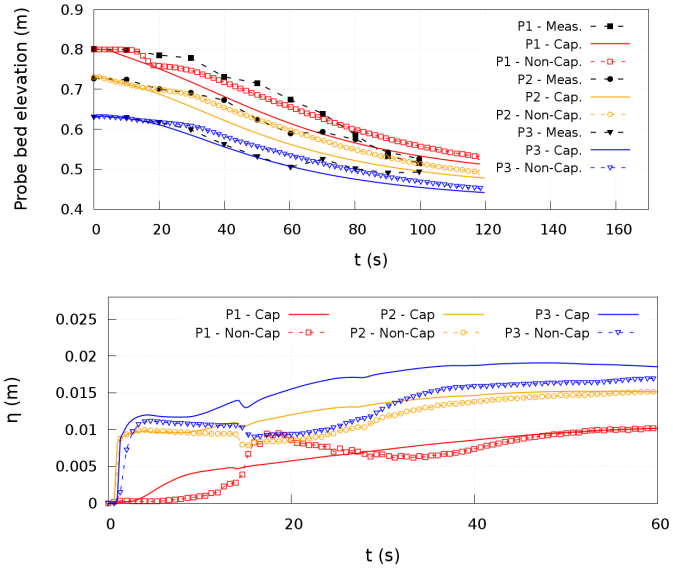

Figure 16: Temporal evolution of the (top) dyke surface elevation and (bottom) active bed layer thickness η for the case C1 at probes P1, P2 and P3. The moving layer thickness has only been plotted for the first 60 sec of simulation.

6.3.2. Case C2

695 Case C2 represents a more challenging benchmark for numerical models. The steeper dyke downward slope leads to a more energetic overtopping flow with elevated erosion rates and also involving stability failures. As in the previous case C1, the best agreement with observed data is achieved with the bedload transport rate computed with the modified Smart-CBFS closure
700 relation. Fig. 17 shows the dyke surface at times $t = 30\,s$ and $t = 60\,s$ after the overflow starts, whereas Fig. 18 depicts the temporal evolutions of the reservoir water level and discharge at the crest. Numerical results considering both equilibrium and non-capacity approaches have been plotted against measured data. The equilibrium condition largely overestimates the

erosion of the dyke surface at the firsts stages after the flow starts, leading to a rapid decrease in the reservoir level and reaching the peak of the discharge hydrograph faster than observed in laboratory (Fig. 18).

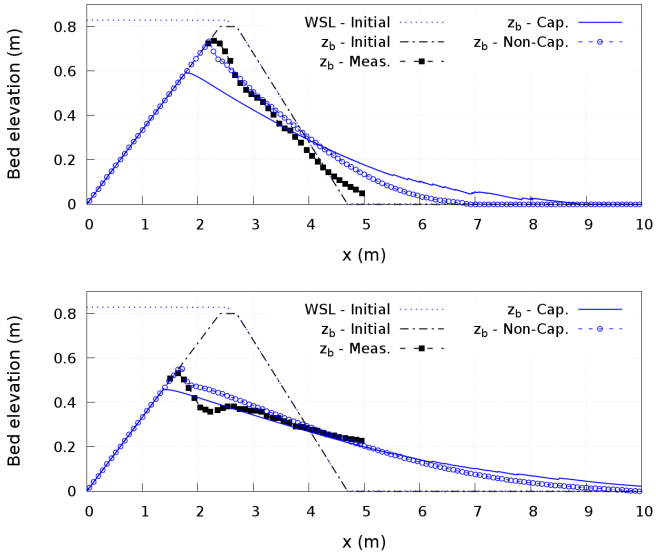

Figure 17: Measured and numerical dyke surfaces at times (top) $t = 30\,s$ and (bottom) $t = 60\,s$ after the overflow starting for the case C2, with modified Smart-CBFS formulation with equilibrium and non-capacity assumption.

	RMSE	
Variable	Capacity	Non-Capacity
WSL_{reserv} (m)	0.11240	0.03808
Q_{crest} (m^3/s)	0.04469	0.01546
z_{b30} (m)	0.10873	0.06024
z_{b60} (m)	0.02792	0.03050

Table 6: RMSE (case C2) for the reservoir level WSL_{reserv}, discharge at the dam crest Q_{crest}, and bed level profiles at times $t = 30\,s$ (z_{b30}) and $t = 60\,s$ (z_{b60}), with capacity and non-capacity formulations.

On the other hand, in general considering non-equilibrium conditions improves the agreement between numerical results and measured data, especially at the first stages after the gate opening. Despite the stability failures

observed at the downward dyke slope during the experiment, the measured and computed dyke surfaces considering the non-equilibrium hypothesis show a good agreement. The root-mean-square error for the non-capacity results were lower for the dyke profile at time $t = 30\,s$ and slightly higher for the time $t = 60\,s$ than those obtained with the capacity bedload transport formulation (Table 6). Furthermore, the non-equilibrium model improved both the reservoir level and the discharge at the dike crest predictions. The root-mean-square error for the reservoir level prediction and the discharge at the dyke crest were much lower with the non-capacity formulation than those obtained considering the equilibrium hypothesis. However, the numerical model considering non-capacity solid transport formulation was not able to properly predict the magnitude of the hydrograph peak observed in laboratory (Fig. 18).

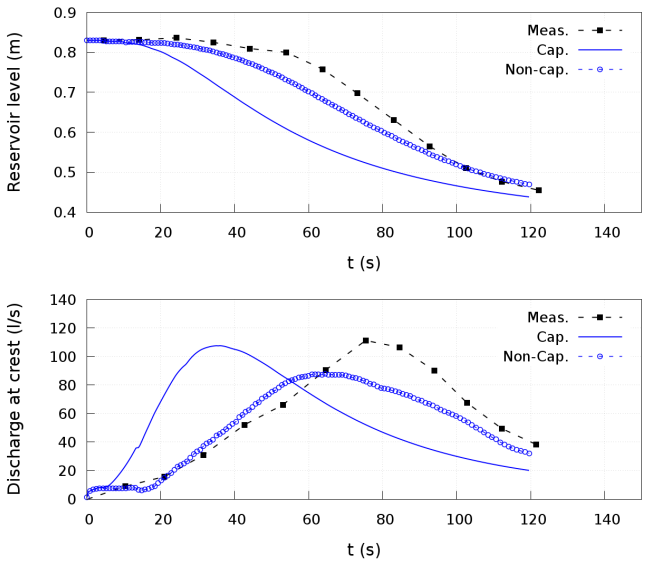

Figure 18: Temporal evolution of the (top) reservoir water surface level and (bottom) discharge at the dyke crest for the case C2, with modified Smart-CBFS formulation with equilibrium and non-capacity assumption.

Finally, Table 7 shows the CPU computational times for tests C1 and C2 using both capacity and non-capacity approaches and the modified Smart-CBFS formula for the determination of the solid transport rate. Differences on computational effort associated to the assumption of capacity or non-capacity formulation can be considered negligible in both benchmark tests.

Formulation	Comp. time (s) Case C1	Case C2
Capacity	49.400	41.199
Non-Capacity	48.288	40.687

Table 7: CPU computational times for cases C1 y C2 with capacity and non-capacity formulations using the Smart-CBFS formula to compute the bedload transport rate.

6.4. Evolution of a trench over non-erodible layer

This experimental benchmark test aims to demonstrate the effectivity of the proposed active control of the sediment thickness positivity method (AC-STP) compared with the classical time step reduction method (TSR) to avoid unphysical over-eroded regions without increasing the required computational cost. The experiments were carried out by Struiksma [43], consisting in the propagation of a trench excavated in a uniform sand bed over a 3 m long non-erodible layer made of a medium gravel (8-16 mm). The experiments were performed in a straight rectangular cross-section flume with an effective length of $11.5\,m$ and a width of $0.20\,m$. The flume was filled with uniform sand ($d_s = 0.45\,mm$, $\rho = 2650 kg/m^3$, $\phi = 32°$ and $p = 0.38$) to a height of 0.15 m above the flume concrete floor, covering also the non-erodible layer. In a first step, a constant discharge was set at the flume inlet and both water and sand were recirculated until uniform bed slope was achieved. The water level was controlled by an adjustable tailgate at the flume outlet. Once a steady bed slope was reached, a 2 m long and 0.04 m deep trench was excavated upstream the gravel layer. The flow was restarted and this bed perturbation propagated downstream, disappearing over the non-erodible layer exposing the gravel stratum and reappearing downstream later. Struiksma [43] proposed a solid transport rate formula $q_s = \kappa\, u^5$ to reproduce the advance velocity of the trench, with κ being a tuning parameter which should be calibrated. Therefore an adapted expression to adjust $G = \kappa\, u^2$ has been derived for the proposed scheme. This case has previously been used for benchmarking by [12, 43, 45, 56] since it reproduces a process of great interest and measured bed elevation data are available.

Two different experimental tests are reproduced in this work, C1 and C2. The main difference between both experiments is that, in C2, the initial sand thickness over the non-erodible layer is lower than in the case C1 and hence the gravel stratum is exposed longer. The cell size for the simulations

is $\Delta x = 0.05m$, the erosion and deposition constant are initially set to $k_e = 2 \cdot 10^{-3}$ and $k_d = 1 \cdot 10^{-5}$ respectively and the CFL is set to 0.95. The flow and sediment transport features used in simulations for both tests have been reported in Table 8 whereas the initial profiles for both the gravel and the erodible layers, as well as the water surface elevation, are shown in Fig. 19:

Case	$q\,inlet\,(l/s)$	$q_s\,inlet\,(l/h)$	$n\,(s/m^3)$	$h_{out}\,(m)$	$\kappa\,(s^4/m^3)$
C1	9.2	7.0	0.019	0.338	0.00020
C2	9.2	4.2	0.019	0.323	0.00022

Table 8: Main parameters used in the simulations for each benchmarking case.

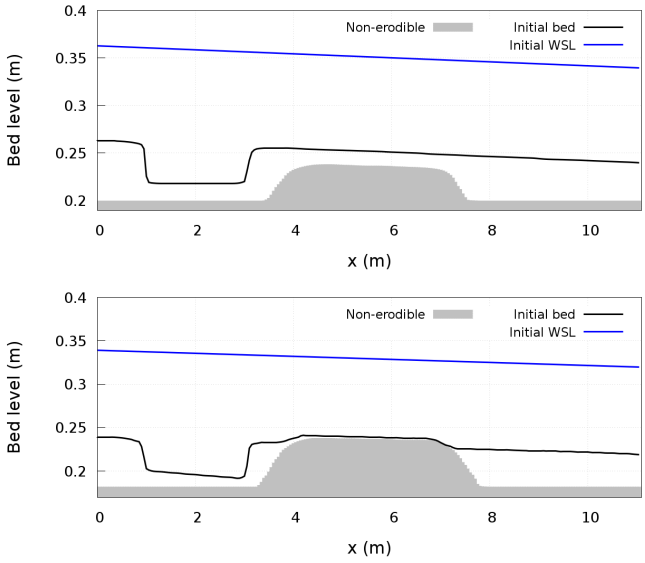

Figure 19: Initial bed and water surface elevations for cases (top) C1 and (bottom) C2.

Fig. 20 depicts the temporal bed evolution for both cases and compares the measured data (black points) with the numerical results obtained by the proposed model, considering non-capacity (point-dashed blue lines) and equilibrium (solid blue lines) approaches. Numerical results obtained with the coupled scheme reported by [22] are also shown (dashed red lines). This model uses the capacity approach for the transport rate determination and the over-erosion problems are controlled by reducing the dynamic time step

to avoid cells with negative sediment thickness values (TSR strategy). The time step reduction is limited to 10% of the value determined by the original CFL condition hence solid mass conservation problems can appear at cells where this reduction is not enough.

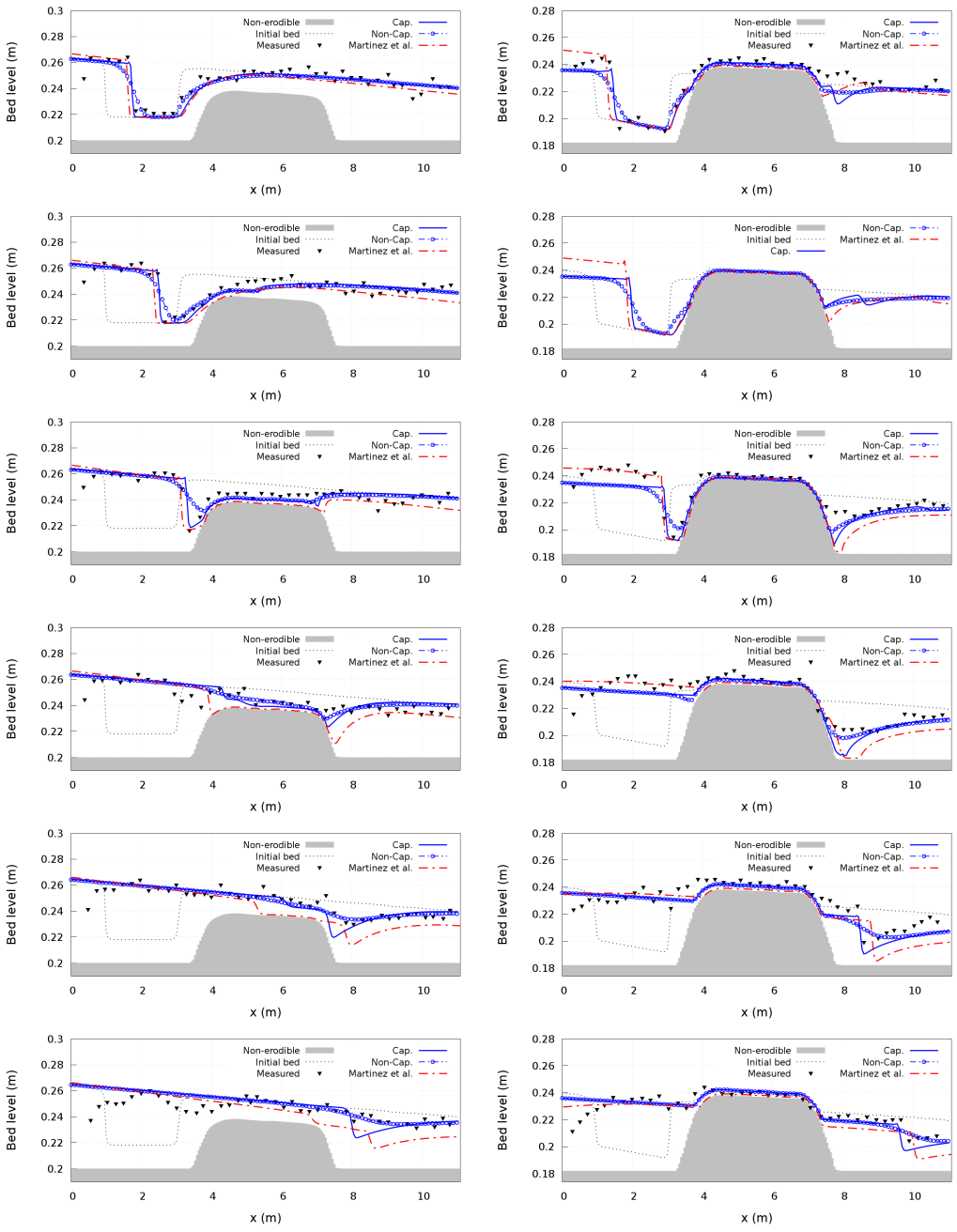

Figure 20: Bed level for (left column) case C1 at times $t = 1\,h, 2\,h, 3\,h, 4\,h, 5\,h, 6\,h$ and (right column) case C2 at times $t = 1\,h, 2\,h, 4\,h, 6\,h, 8\,h, 10\,h$.

The scheme proposed in this work is able to reproduce the trench propagation process over the gravel stratum, considering both equilibrium and non-capacity conditions. The non-capacity approach with $k_e = 2 \cdot 10^{-3}$ seems to introduce an extra-diffusion term on the numerical solution comparing with the equilibrium approach, although the trench propagation velocity is similar and agreeing with the observed data for both tests. The present model using the AC-STP method to avoid over-erosion was able to improve largely the prediction of the trench propagation obtained with the scheme reported in [22] using the TSR strategy (see Table 9).

	RMSE z_b (m)	
Formulation	Case C1	Case C2
Capacity	0.00651	0.00685
Non-Capacity	0.00621	0.00654
Martínez et al.	0.00911	0.00847

Table 9: RMSE (cases C1 y C2) for the bed level evolution z_b, with capacity and non-capacity formulations. Also RMSE for the results obtained with the Martínez et al. model [22] has been reported.

Furthermore, most numerical models dealing with these cases [12, 45, 56] predict an excavated region downstream the gravel stratum which was not observed in experiments. That excavated zone is also reproduced here using the equilibrium model [22] with the classical time-reduction (TSR) treatment for the non-erodible layer. The present non-capacity formulation ($k_e = 2 \cdot 10^{-3}$) is able to eliminate totally this excavation for case C1 and to reduce it significantly for case C2. The solid transport q_s over the gravel stratum is reduced as an effect of the sediment unavailability using (51). This reduction interferes with the equivalent non-equilibrium adaptation length, leading to a solid transport rate smaller than the flow transport capacity downstream the gravel stratum. Therefore, the solid transport rate at the downstream region is lower with non-capacity formulation than that considering the equilibrium hypothesis, reducing the excavation.

Fig. 21 shows the effects of the erosion constant k_e increase on the evolution of the excavated region downstream the gravel stratum. Lower erosion constant k_e values lead to an increment of the equivalent adaptation length (13). The reduction of the physical solid transport rate applied in cells where the theoretical active layer thickness η is greater than the avail-

able sediment thickness ϵ_b leads to a more stable propagation of the trench over the gravel stratum and reduces the excavated region downstream. As the erosion constant k_e increases, the equivalent adaptation length decreases and the non-equilibrium solid transport states caused by the appearance of the non-erodible layer are also reduced. Hence, the non-capacity solution tends approximate to the equilibrium bed evolution profile (see Fig. 21). With $k_e = 2 \cdot 10^{-2}$ the non-capacity results practically agree with the equilibrium prediction, demonstrating the sensitivity of the model to the erosion-deposition constants calibration.

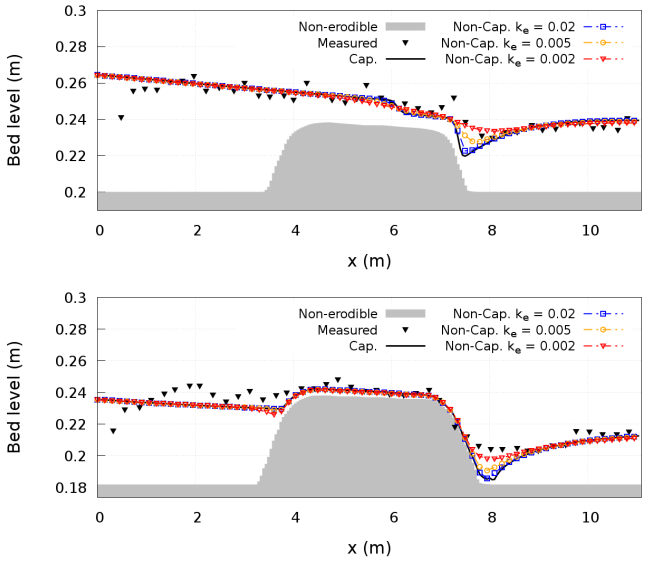

Figure 21: Bed level for (top) case C1 at time $t = 5\,h$ and (bottom) case C2 at time $t = 6\,h$ with non-capacity formulation.

Finally, the positivity control mechanism for the sediment thickness, (61) and (62), is triggered many times during simulations as the gravel stratum is successively exposed and recovered during the trench advance. In order to demonstrate the effectiveness of the AC-STP method, additional simulations were carried out considering the proposed model but using the classical TSR strategy to avoid unphysical over-eroded cells, using both equilibrium and non-equilibrium hypothesis. Fig. 22 shows the bed profiles for case C1 at $t = 3\,h$ and case C2 at $t = 4\,h$, times when the whole gravel stratum was exposed. The bed level predictions computed with capacity AC-STP and capacity TSR methods showed small variations caused by the different treatment of

non-erodible stratum. Similar small variations were found comparing non-capacity AC-STP and non-capacity TSR methods. However, using the AC-STP method the numerical solution remains stable and it is not necessary to reduce the time step to ensure the sediment mass conservation or numerical stability (Fig. 23), unlike using TSR method [45]. Furthermore, the time step reduction strategy demonstrates not to be able to avoid completely the over-erosion problems without a marked reduction of the time step, leading to much a higher computational effort for the simulations (Table 10). Moreover, as the time step reduction is limited to avoid an excessive computational effort, solid mass conservation errors appear in cells which require higher limitations to remain positive sediment thickness values.

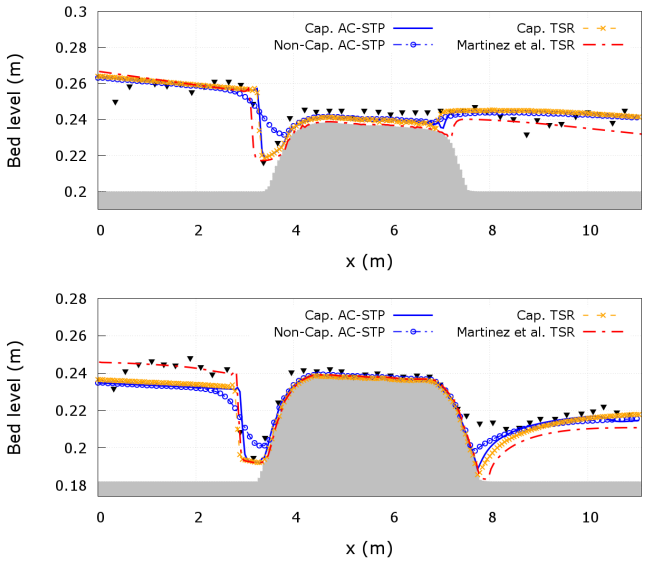

Figure 22: Bed level for (left) case C1 at time $t = 3\,h$ and (right) case C2 at time $t = 4\,h$ using non-capacity AC-STP, non-capacity TSR, capacity TSR and Martínez et al. TSR models.

Formulation	Comp. time (s) Case C1	Case C2
Capacity AC-STP	134.144	225.748
Capacity TSR	253.478	757.296
Non-Capacity AC-STP	133.528	232.663
Non-Capacity TSR	202.018	448.121
Martínez et al. TSR	463.105	921.838

Table 10: CPU computational times (cases C1 y C2) for capacity AC-STP, capacity TSR, non-capacity AC-STP and non-capacity TSR models. Also the computational time for Martínez et al. TSR model [22] has been reported.

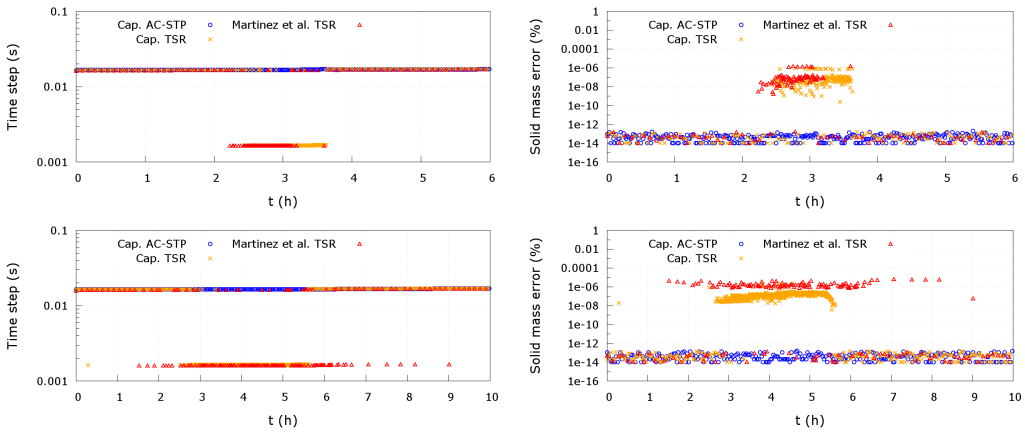

Figure 23: Dynamic time step (left column) and solid mass conservation errors (right column) for cases (top) C1 and (bottom) C2. Note that results are shown for every 20 time steps. For the sake of clarity only results using capacity formulation have been depicted.

7. Conclusions

In this work, recently developed non-equilibrium bedload transport concepts have been used to propose a new numerical model able to deal with highly unsteady flows and partially non-erodible bed layers. Based on a grain-scale analysis of the net exchange flux through the static-moving bed layers interface [41], new expressions for the erosion and deposition rates ($\dot{\eta}_e$ and $\dot{\eta}_d$, respectively) have been obtained, as well as a generalized formula for the non-capacity bedload transport rate q_s as a function of the active layer

thickness η. The equilibrium state consists of a particular case of the generalized bedload formulation derived. The proposed transport rate formulation allows to limit the physical solid flux at cells in regions where the total sediment thickness ϵ_b hinders the development of equilibrium solid transport states. A new generalized Grass-type formulation is proposed for the non-equilibrium bedload transport rate. This is the first of the main novelties reported in the present work.

The system of equations composed by the one-dimensional shallow water and the mass conservation equations for the bed layer (4 equations) has been solved using a first order finite volume A-Roe scheme. The convective flux vector is separated in a part accounting for the flow depending terms plus a corrector component associated to the Grass factor G variation. The second novelty of the present work is this upwind splitting of the convective solid flux. An improved reconstruction strategy for the approximated solution at each local RP allows to avoid the appearance of unphysical results in the erodible layer thickness ϵ_b, one of the most important problems reported for equilibrium and non-equilibrium bedload numerical models dealing with non-erodible layers [12, 45]. This new reconstruction strategy is the third novelty presented in this work.

Currently, a high uncertainty exists about the calibration of the non-capacity parameters (erosion-deposition constants, k_e and k_d, or adaptation length L_b in other models [25, 27, 37]) and their effect on numerical predictions. The model has been tested against a hypothetical case consisting of a rectangular dune made of non-cohesive sand moving over a non-erodible bed layer. The sensitivity of the numerical evolution of the dune surface to the non-capacity parameters calibration has been analysed. One of our conclusions is that the relation k_e/k_d controls the active layers thickness and hence the mean velocity at the moving sediment layer. Furthermore, the reduction of k_e leads to increasing non-equilibrium conditions, as it happens with the adaptation length L_b increments in flux relaxation models. The highest k_e, the fastest the bedload solid transport is able to achieve equilibrium states, even for constant k_e/k_d relation.

The proposed model has been benchmarked against different sediment transport laboratory experiments, involving unsteady flows, enhanced bed changes by light-weight sediments and underlying non-erodible layers scour. The model is able to predict the measured data in all the cases tested. The non-equilibrium bedload transport assumption improves the results obtained in most of the cases, especially for the dyke-breaking by overtopping bench-

marking test (6.3) and the trench propagation over a non-erodible layer test (6.4). However, the numerical results obtained are very sensitive to the calibration of the non-capacity parameters, which can become a difficult task. On the other hand, the proposed reconstruction strategy to avoid negative values in the sediment thickness ϵ_b demonstrates to improve the results obtained with the classical numerical fixes used up till now for cases involving finite-depth erodible layers, regardless of equilibrium or non-equilibrium approaches. This technique allows to ensure the solid mass conservation property allowing numerical stability with time steps larger than other approaches and hence improves the computational efficiency of scheme.

Acknowledgements

This work was partially funded by the MINECO/FEDER under research project CGL2015-66114-R and by Diputacion General de Aragon, DGA, through Fondo Europeo de Desarrollo Regional, FEDER.

References

[1] C. Yang, Sediment Transport: Theory and Practice, McGraw-Hill Inc., New York, 1996.

[2] W. Wu, Computational River Dynamics, NetLibrary, Inc, CRC Press, 2007.

[3] B. Spinewine, Y. Zech, Small-scale laboratory dam-break waves on movable beds, Journal of Hydraulic Research 45 (sup1) (2007) 73–86.

[4] Y. Zech, S. Soares-Frazo, B. Spinewine, N. L. Grelle, Dam-break induced sediment movement: Experimental approaches and numerical modelling, Journal of Hydraulic Research 46 (2) (2008) 176–190.

[5] I. Fent, Y. Zech, S. Soares-Frazo, Dam-break flow experiments over mobile bed: velocity profile, Journal of Hydraulic Research 57 (1) (2019) 131–138.

[6] M. Wong, G. Parker, Reanalysis and Correction of Bed-Load Relation of Meyer-Peter and Müller Using Their Own Database, Journal of Hydraulic Engineering 132 (11) (2006) 1159–1168.

[7] J. Pitlick, R. Cress, Downstream changes in channel geometry of a large gravel bed river, Water Resources Research 38 (10) (2002) 34–1.

[8] S. Soares-Frazão, N. LeGrelle, B. Spinewine, Y. Zech, Dam-break induced morphological changes in a channel with uniform sediments: measurements by a laser-sheet imaging technique, Journal of Hydraulic Research 45 (sup1) (2007) 8795.

[9] G. Brooks, D. Lawrence, The drainage of the Lake Ha!Ha! reservoir and downstream geomorphic impacts along Ha!Ha! River, Saguenay area, Quebec, Canada, Geomorphology 28 (1) (1999) 141 – 167.

[10] A.-J.-C. Saint-Venant, Théorie du mouvement non permanent des eaux, avec application aux crues des rivires et à l'introduction des marées dans leur lit, Comptes rendus hebdomadaires des séances de l'Académie des sciences, France 73 (1871) 11.

[11] J. Cunge, F. Holly, A. Verwey, Practical aspects of computational river hydraulics, Monographs and surveys in water resources engineering, Pitman Advanced Publishing Program, 1980.

[12] B. Dewals, F. Rulot, S. Erpicum, P. Archambeau, M. Pirotton, Advanced Topics in Sediment Transport Modelling: Non-alluvial Beds and Hyperconcentrated Flows, in: S. S. Ginsberg (Ed.), Sediment Transport, chap. 1, IntechOpen, Rijeka, Croatia, 2011.

[13] T. Tingsanchali, C. Chinnarasri, Numerical modelling of dam failure due to flow overtopping, Hydrological Sciences Journal 46 (1) (2001) 113–130.

[14] Z. Cao, R. Day, S. Egashira, Coupled and Decoupled Numerical Modeling of Flow and Morphological Evolution in Alluvial Rivers, Journal of Hydraulic Engineering 128 (3) (2002) 306–321.

[15] D. Lyn, M. Altinakar, St. Venant-Exner Equations for Near-Critical and Transcritical Flows, Journal of Hydraulic Engineering 128 (6) (2002) 579–587.

[16] J. Hudson, P. K. Sweby, Formulations for Numerically Approximating Hyperbolic Systems Governing Sediment Transport, Journal of Scientific Computing 19 (1) (2003) 225–252.

[17] L. Goutière, S. Soares-Frazão, C. Savary, T. Laraichi, Y. Zech, One-Dimensional Model for Transient Flows Involving Bed-Load Sediment Transport and Changes in Flow Regimes, Journal of Hydraulic Engineering 134 (6) (2008) 726–735.

[18] M. Castro-Díaz, E. Fernández-Nieto, A. Ferreiro, Sediment transport models in Shallow Water equations and numerical approach by high order finite volume methods, Computers & Fluids 37 (3) (2008) 299 – 316.

[19] J. Murillo, P. Garcia-Navarro, An Exner-based coupled model for two-dimensional transient flow over erodible bed, Journal of Computational Physics 229 (23) (2010) 8704–8732.

[20] C. Juez, J. Murillo, P. García-Navarro, A 2D weakly-coupled and efficient numerical model for transient shallow flow and movable bed, Advances in Water Resources 71 (2014) 93 – 109.

[21] P. Gunawan, X. Lhébrard, Hydrostatic relaxation scheme for the 1D shallow water - Exner equations in bedload transport, Computers & Fluids 121 (2015) 44 – 50.

[22] S. Martínez-Aranda, J. Murillo, P. García-Navarro, A 1D numerical model for the simulation of unsteady and highly erosive flows in rivers, Computers & Fluids 181 (2019) 8–34.

[23] A. Armanini, G. Di Silvio, A one-dimensional model for the transport of a sediment mixture in non-equilibrium conditions, Journal of Hydraulic Research 26 (3) (1988) 275–292.

[24] L. Fraccarollo, H. Capart, Y. Zech, A Godunov method for the computation of erosional shallow water transients, International Journal for Numerical Methods in Fluids 41 (9) (2003) 951–976.

[25] W. Wu, S. Wang, One-Dimensional Modeling of Dam-Break Flow over Movable Beds, Journal of Hydraulic Engineering 133 (1) (2007) 48–58.

[26] K. El Kadi Abderrezzak, A. Paquier, One-dimensional numerical modeling of sediment transport and bed deformation in open channels, Water Resources Research 45 (5).

[27] S. Zhang, J. Duan, 1D finite volume model of unsteady flow over mobile bed, Journal of Hydrology 405 (1) (2011) 57 – 68.

[28] F. Benkhaldoun, S. Sari, M. Seaid, A flux-limiter method for dam-break flows over erodible sediment beds, Applied Mathematical Modelling 36 (10) (2012) 4847 – 4861.

[29] Z. Cao, Z. Li, G. Pender, P. Hu, Non-capacity or capacity model for fluvial sediment transport, Proceedings of the Institution of Civil Engineers - Water Management 165 (4) (2012) 193–211.

[30] E. Fernández-Nieto, C. Lucas, T. Morales-de Luna, S. Cordier, On the influence of the thickness of the sediment moving layer in the definition of the bedload transport formula in Exner systems, Computers & Fluids 91 (2014) 87 – 106.

[31] X. Liu, A. Mohammadian, A. Kurganov, J. Infante-Sedano, Well-balanced central-upwind scheme for a fully coupled shallow water system modeling flows over erodible bed, Journal of Computational Physics 300 (2015) 202 – 218.

[32] P. Bohorquez, C. Ancey, Particle diffusion in non-equilibrium bedload transport simulations, Applied Mathematical Modelling 40 (17) (2016) 7474 – 7492.

[33] Multiple time scales of alluvial rivers carrying suspended sediment and their implications for mathematical modeling, Advances in Water Resources 30 (4) (2007) 715 – 729.

[34] L. Van-Rijn, Principles of sediment transport in rivers, estuaries and coastal seas, chap. 10, Bed material transport, erosion and deposition in non-steady and non-uniform flow, Aqua Publications, Amsterdam, 1993.

[35] Z. Cao, P. Hu, G. Pender, Multiple Time Scales of Fluvial Processes with Bed Load Sediment and Implications for Mathematical Modeling, Journal of Hydraulic Engineering 137 (3) (2011) 267–276.

[36] K. El Kadi Abderrezzak, A. Paquier, B. Gay, One-dimensional numerical modelling of dam-break waves over movable beds: application to experimental and field cases, Environmental Fluid Mechanics 8 (2) (2008) 169–198.

[37] M. R. Soliman, S. Ushijima, Equilibrium and Non-equilibrium Sediment Transport Modeling Based On Parallel MACS Algorithm, Journal of Japan Society of Civil Engineers 69 (2) (2013) 79–86.

[38] L. van Rijn, Sediment Transport, Part I: Bed Load Transport, Journal of Hydraulic Engineering 110 (10) (1984) 1431–1456.

[39] H. Lee, I. Hsu, Investigation of Saltating Particle Motions, Journal of Hydraulic Engineering 120 (7) (1994) 831–845.

[40] R. M. L. Ferreira, M. J. Franca, J. G. A. B. Leal, A. H. Cardoso, Mathematical modelling of shallow flows: Closure models drawn from grain-scale mechanics of sediment transport and flow hydrodynamics 36 (10) (2009) 1605–1621.

[41] F. Charru, Selection of the ripple length on a granular bed sheared by a liquid flow, Physics of Fluids 18 (12) (2006) 121508.

[42] E. D. Fernández-Nieto, T. M. d. Luna, G. Narbona-Reina, J. d. D. Zabsonré, Formal deduction of the Saint-Venant-Exner model including arbitrarily sloping sediment beds and associated energy, Mathematical Modelling and Numerical Analysis 51 (1) (2017) 115–145.

[43] N. Struiksma, Mathematical modelling of bedload transport over non-erodible layers, in: IAHR symposium on River, Coastal amd Estuarine Morphodynamics, Genova, Italy, 89–98, 1999.

[44] F. Rulot, B. Dewals, S. Erpicum, P. Archambeau, M. Pirotton, Modelling sediment transport over partially non-erodible bottoms, International Journal for Numerical Methods in Fluids 70 (2) (2012) 186–199.

[45] D. Caviedes-Voullième, M. Morales-Hernndez, C. Juez, A. Lacasta, P. García-Navarro, Two-Dimensional Numerical Simulation of Bed-Load Transport of a Finite-Depth Sediment Layer: Applications to Channel Flushing, Journal of Hydraulic Engineering 143 (9) (2017) 04017034.

[46] J. Murillo, P. García-Navarro, Weak Solutions for Partial Differential Equations with Source Terms: Application to the Shallow Water Equations, J. Comput. Phys. 229 (11) (2010) 4327–4368.

[47] J. Murillo, A. Navas-Montilla, A comprehensive explanation and exercise of the source terms in hyperbolic systems using Roe type solutions. Application to the 1D-2D shallow water equations, Advances in Water Resources 98 (2016) 70 – 96.

[48] E. Meyer-Peter, R. Müller, Formulas for Bed-Load Transport, in: Report on 2nd meeting on international association on hydraulic structures research, Stockholm, Sweden, 39–64, 1948.

[49] P. Nielsen, Coastal Bottom Boundary Layers and Sediment Transport, Advanced series on ocean engineering, World Scientific, 1992.

[50] R. F. Luque, R. V. Beek, Erosion And Transport Of Bed-Load Sediment, Journal of Hydraulic Research 14 (2) (1976) 127–144.

[51] G. Smart, Sediment transport formula for steep channels, Journal of Hydraulic Engineering 3 (1984) 267–276.

[52] F. Exner, Über die Wechselwirkung zwischen Wasser und Geschiebe in Flüssen: Gedr. mit Unterstütz aus d. Jerome u. Margaret Stonborough-Fonds, Akademie der Wissenschaften, Wien, 1925.

[53] W. Wu, D. Vieira, S. Wang, One-Dimensional Numerical Model for Nonuniform Sediment Transport under Unsteady Flows in Channel Networks, Journal of Hydraulic Engineering 130 (9) (2004) 914–923.

[54] S. Godunov, A Difference Scheme for Numerical Solution of Discontinuous Solution of Hydrodynamic Equations, Math. Sbornik 47 (1959) 271–306.

[55] E. Toro, Riemann Solvers and Numerical Methods for Fluid Dynamics: A Practical Introduction, Springer, Berlin, Germany, 1997.

[56] P. Ortiz, J. Anguita, M. Riveiro, Free surface flows over partially erodible beds by a continuous finite element method, Environmental Earth Sciences 74 (11) (2015) 7357–7370.

[57] E. Lajeunesse, L. Malverti, F. Charru, Bed load transport in turbulent flow at the grain scale: Experiments and modeling, Journal of Geophysical Research: Earth Surface 115 (2010) F04001.

[58] A. Paquier, K. El Kadi, A Model for Bed-Load Transport and Morphological Evolution in Rivers: Description and Pertinence, in: S. Benzoni-Gavage, D. Serre (Eds.), Hyperbolic Problems: Theory, Numerics, Applications, Springer Berlin Heidelberg, Berlin, Heidelberg, 285–296, 2008.

[59] C. Juez, J. Murillo, P. Garcia-Navarro, Numerical assessment of bedload discharge formulations for transient flow in 1D and 2D situations, Journal of Hydroinformatics 15 (4) (2013) 1234–1257.

[60] R. Bagnold, The nature of saltation and of bed-load transport in water, Proceedings of the Royal Society of London. A. Mathematical and Physical Sciences 332 (1591) (1973) 473–504.

Appendix A. Erosion and deposition rates derivation

The derivation of the expressions used in this work for the erosion and deposition rates, $\dot{\eta}_e$ and $\dot{\eta}_d$ respectively, was based on the physical background proposed by Charru [41] for the net exchange flux between the static and moving bed layers.

Appendix A.1. Deposition rate

The particle deposition rate $\dot{n}_d$ is related to the number of moving particles n and the characteristic deposition time t_d:

$$\dot{n}_d = \frac{n}{t_d} \qquad \left[Part.T^{-1}\right] \tag{A.1}$$

The characteristic time of the deposition process is controlled by gravity and depends on the deposition velocity ω_s and the particle diameter d_s:

$$\begin{aligned} \frac{1}{t_d} &\propto \frac{\omega_s}{d_s} \\ \frac{1}{t_d} &= k_d \frac{\sqrt{(s-1)gd_s}}{d_s} \end{aligned} \tag{A.2}$$

and hence the particle deposition rate can be expressed as:

$$\dot{n}_d = k_d \frac{n}{d_s} \frac{\sqrt{(s-1)gd_s^3}}{d_s} \tag{A.3}$$

being k_d a deposition constant.

On the other hand, the number of particles in movement on a bed surface of unit area $\delta A = \delta x\, \delta y = 1$ and which are affected by deposition in a time step t_d are related to the thickness of the active bedload layer η:

$$n = \frac{\eta\, \delta A}{\xi d_s^3} \tag{A.4}$$

where $\xi = 1/(1-p)$, being p the porosity of the active layer which is considered the same as the static layer.

The relation between the particle deposition rate and the temporal variation of the active layer thickness due to deposition in a bed area δA is expressed as:

$$\dot{\eta}_d = \frac{\dot{n}_d\, \xi d_s^3}{\delta A} \tag{A.5}$$

Therefore, replacing A.4 and A.5 in A.3, the temporal variation of the moving layer thickness due to deposition can be expressed as:

$$\dot{\eta}_d = k_d \frac{\eta}{d_s} \frac{\sqrt{(s-1)g d_s^3}}{d_s} \qquad \left[L\,T^{-1}\right] \tag{A.6}$$

Appendix A.2. Erosion rate

The particle erosion rate $\dot{n}_e$ is related to the number n of static particles exposed to the flow action and the characteristic erosion time t_e:

$$\dot{n}_e = \frac{n}{t_e} \qquad \left[Part.\,T^{-1}\right] \tag{A.7}$$

The particles which are exposed to the flow shear stress in a bed surface of unit area $\delta A = \delta x\,\delta y = 1$ and which can be incorporated to the moving layer in a time step t_e are placed on the top layer of the static sediment column and hence:

$$n = \frac{d_s\,\delta A}{\xi d_s^3} \quad \rightarrow \quad \dot{n}_e = \frac{\delta A}{t_e\,\xi d_s^2} \tag{A.8}$$

The characteristic erosion time t_e for turbulent flow is proportional to the inertial balance between the settling momentum of the sediment particles and the stress forces exerted by the flow on them:

$$\begin{aligned} \frac{1}{t_e} &\propto \frac{(\tau - \tau_c)_+\, d_s^2}{\rho_s d_s^3\, \omega_s} \\ \frac{1}{t_e} &= k_e \frac{(\theta - \theta_c)_+}{s\, d_s} \sqrt{(s-1) g d_s} \end{aligned} \tag{A.9}$$

being $s = \rho_s/\rho_w$ the relative density of the sediment particles, $\theta = |\tau|/(\rho_s - \rho_w) g d_s$ the non-dimensional Shields stress, θ_c the critical value of the Shields stress for the incipient motion, τ the shear stress at the bed surface and k_e an erosion constant. The symbol $()_+$ indicates that the function only has values along the positive domain and is nil for the negative domain.

Taking into account that the relation between the temporal variation of the moving layer thickness and the flux of sediment particles involved in the erosive process in a bed area δA can be written as:

$$\dot{\eta}_e = \frac{\dot{n}_e\,\xi d_s^3}{\delta A} \tag{A.10}$$

the temporal evolution of the bed-load layer thickness caused by erosion can be expressed as:

$$\dot{\eta}_e = k_e \frac{(\theta - \theta_c)_+}{s} \frac{\sqrt{(s-1) g d_s^3}}{d_s} \qquad \left[L\,T^{-1}\right] \tag{A.11}$$

Note that for the capacity case in which the erosion and deposition rates are equal ($\dot{\eta}_e = \dot{\eta}_d$), the relation $n\,d_s^2 \propto (\theta - \theta_c)_+$ is recovered. This linear relation for the number of particles in the moving layer agrees with the experimental observations reported by Luque and Beek [50] and Bagnold [60], and is used to derived most of the classical solid transport rate reported in literature.

Appendix B. Properties of the edge-averaged Grass parameter $\widetilde{\mathbf{G}}$

To explore the upwind behaviour of the edge-averaged Grass factor $\widetilde{G}_{i+\frac{1}{2}}$ (32), in this appendix its value has been analysed in some numerical situations.

Constant Grass parameter in left and right cells

If both cells have equal interaction parameter, then the edge averaged Grass parameter is constant along the edge:

$$G_i = G_{i+1} = \widetilde{G}_{i+\frac{1}{2}}$$

regardless of the flow conditions and hence the corrector flux vector $\delta\widetilde{F}^G_{i+\frac{1}{2}}$ are nil.

Transitions with non-erodible layers

Supposing that the interaction parameter at the right cell is nil ($G_{i+1} = 0$), then the edge-average Grass factor can be expressed as:

$$\widetilde{G}_{i+\frac{1}{2}} = \frac{G_i h_{i+1}^{3/2}}{(\sqrt{h_i} + \sqrt{h_{i+1}})^3} + \frac{3G_i(\sqrt{h_i} h_{i+1} + h_i\sqrt{h_{i+1}})u_i^2 + 3G_i\sqrt{h_i} h_{i+1} u_i u_{i+1}}{(\sqrt{h_i} + \sqrt{h_{i+1}})^3\,(u_i^2 + u_{i+1}^2 + u_i u_{i+1})} \tag{B.1}$$

Considering uniform flow ($h_i = h_{i+1}$ and $u_i = u_{i+1}$) the only factor which could cause a null Grass factor at the cell $i+1$ (and not at cell i) is the

unavailability of sediment at the cell. Under these conditions, the edge-averaged interaction parameter is:

$$\widetilde{G}_{i+\frac{1}{2}} = \frac{G_i}{2}$$

and hence the corrector flux vector:

$$\delta\widetilde{F}^{G-}_{i+\frac{1}{2}} = \left(0,\, 0,\, -\xi\widetilde{u}\frac{G_i}{2}\right)^T$$
$$\delta\widetilde{F}^{G+}_{i+\frac{1}{2}} = \left(0,\, 0,\, -\xi\widetilde{u}\frac{G_i}{2}\right)^T$$

Dambreak wave front on wet conditions

The advance of an erosive dambreak wave on a wet bed is characterized by the following local flow conditions:

$$h_i > 0,\, u_i > 0,\, G_i > 0$$
$$h_{i+1} > 0,\, u_{i+1} = 0,\, G_{i+1} = 0$$

In that case, the edge-averaged Grass parameter has the following expression:

$$\widetilde{G}_{i+\frac{1}{2}} = G_i\left(1 - \frac{h_i^{3/2}}{(\sqrt{h_i} + \sqrt{h_{i+1}})^3}\right) \tag{B.2}$$

depending only on the water depth values at the left and right cells. In the limiting case where $h_i = h_{i+1}$, the Grass parameter takes the value

$$\widetilde{G}_{i+\frac{1}{2}} = \frac{7}{8}G_i$$

and hence the corrector flux vector:

$$\delta\widetilde{F}^{G-}_{i+\frac{1}{2}} = \left(0,\, 0,\, -\xi\widetilde{u}\frac{1}{8}G_i\right)^T$$
$$\delta\widetilde{F}^{G+}_{i+\frac{1}{2}} = \left(0,\, 0,\, -\xi\widetilde{u}\frac{7}{8}G_i\right)^T$$

Dambreak wave front on dry conditions

The advance of an erosive dambreak wave on a dry bed, the local flow conditions are:

$$h_i > 0,\ u_i > 0,\ G_i > 0$$
$$h_{i+1} = 0,\ u_{i+1} = 0,\ G_{i+1} = 0$$

Therefore, the edge-averaged Grass factor is nil, $\widetilde{G}_{i+\frac{1}{2}} = 0$, and the corrector flux vector:
and hence the corrector flux vector:

$$\delta\widetilde{F}^{G-}_{i+\frac{1}{2}} = (0,\ 0,\ -\xi\widetilde{u}G_i)^T$$
$$\delta\widetilde{F}^{G+}_{i+\frac{1}{2}} = (0,\ 0,\ 0)^T$$

Appendix C. Eigenvalues, wave and source strength derivation

Appendix C.1. Eigenvalues calculation

The eigenvalues of the linearized matrix $\widetilde{\mathbf{M}}_{i+\frac{1}{2}}$ are calculated as the roots of its characteristic polynomial $P_{\widetilde{M}}(\widetilde{\lambda})$:

$$P_{\widetilde{M}}(\widetilde{\lambda}) = -\widetilde{\lambda}^3 + 2\widetilde{u}\widetilde{\lambda}^2 + \left(\widetilde{c}^2 - \widetilde{u}^2 + \widetilde{c}^2\xi\widetilde{G}\widetilde{d}\right)\widetilde{\lambda} - \widetilde{c}^2\widetilde{u}\,\xi\widetilde{G}\widetilde{d} = 0$$

which can be rewritten as:

$$P_{\widetilde{M}}(\widetilde{\lambda}) = \widetilde{\lambda}^3 + a_1\widetilde{\lambda}^2 + a_2\widetilde{\lambda} + a_3 = 0$$

with: $a_1 = -2\widetilde{u} \qquad a_2 = \widetilde{u}^2 - \widetilde{c}^2 - \widetilde{c}^2\xi\widetilde{G}\widetilde{d} \qquad a_3 = \widetilde{c}^2\widetilde{u}\,\xi\widetilde{G}\widetilde{d}$

Using the *Cardano-Vieta* formula, the eigenvalues are calculated as:

$$\widetilde{\lambda}_1 = 2\sqrt{-L}\ cos(\phi/3) - a_1/3$$
$$\widetilde{\lambda}_2 = 2\sqrt{-L}\ cos(\phi/3 + 2\pi/3) - a_1/3$$
$$\widetilde{\lambda}_3 = 2\sqrt{-L}\ cos(\phi/3 + 4\pi/3) - a_1/3$$

where:

$$L = \frac{3a_2 - a_1^2}{9} \qquad \phi = acos\left(\frac{R}{\sqrt{-L^3}}\right) \qquad R = \frac{9a_1a_2 - 27a_3 - 2a_1^3}{54}$$

Appendix C.2. Wave strengths

Conserved variable spatial increments at each intercell edge $i+\frac{1}{2}$ can be projected onto the right eigenvector base, obtaining the wave strengths $\widetilde{\alpha}_m$ at that edge:

$$\delta U_{i+\frac{1}{2}} = \begin{pmatrix} \delta h \\ \delta q \\ \delta \epsilon_b \end{pmatrix}_{i+\frac{1}{2}} = \sum_m \widetilde{\alpha}_m \vec{\widetilde{e}}_m$$

$$\widetilde{\alpha}_m = \frac{\left(\widetilde{c}^2 - \widetilde{u}^2 + \prod_{k\neq m} \widetilde{\lambda}_k\right) \delta h + \left(2\widetilde{u} - \sum_{k\neq m} \widetilde{\lambda}_k\right) \delta q + \widetilde{c}^2 \, \delta \epsilon_b}{\widetilde{\lambda}_m \left(\widetilde{\lambda}_m - \sum_{k\neq m} \widetilde{\lambda}_k\right) + \prod_{k\neq m} \widetilde{\lambda}_k} \tag{C.1}$$

Appendix C.3. Source strengths

Source terms are integrated over a suitable control volume for each local Riemann problem. Then, the result is projected onto the right eigenvectors basis as a function of the Roe's average quantities at the intercell edge.

$$\widetilde{\mathbf{S}}_{i+\frac{1}{2}} = \begin{pmatrix} \widetilde{S}_1 \\ \widetilde{S}_2 \\ \widetilde{S}_3 \end{pmatrix}_{i+\frac{1}{2}} = \begin{pmatrix} 0 \\ -g\bar{h}\,\delta z_R - g\bar{h}\widetilde{S}_f\,\delta x \\ 0 \end{pmatrix}_{i+\frac{1}{2}} = \sum_m \widetilde{\beta}_m \vec{\widetilde{e}}_m$$

$$\widetilde{\beta}_m = \frac{\left(2\widetilde{u} - \sum_{k\neq m} \widetilde{\lambda}_k\right) \widetilde{S}_2}{\widetilde{\lambda}_m \left(\widetilde{\lambda}_m - \sum_{k\neq m} \widetilde{\lambda}_k\right) + \prod_{k\neq m} \widetilde{\lambda}_k} \tag{C.2}$$

Appendix D. Solid flux intermediate states at the intercell edge

From (45), the numerical solid fluxes associated to both the left and the right intermediate states at the intercell edge $i+\frac{1}{2}$ (Fig. D.24) can be expressed as:

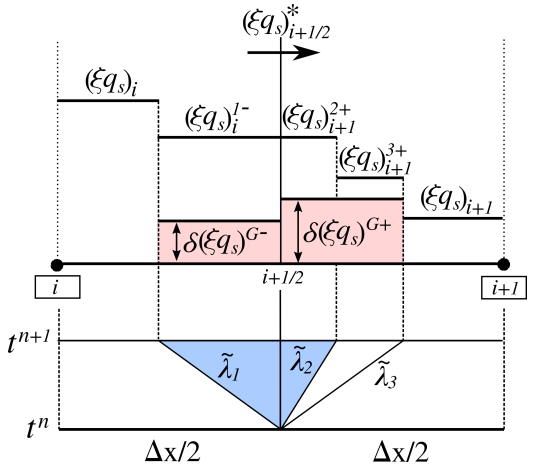

Figure D.24: Intermediate states for the solid discharge $\xi\, q_s$ at the intercell edge $i + \frac{1}{2}$.

$$
\begin{aligned}
F^{-}_{3,\,i} &\equiv (\xi q_s)^{1-}_i = (\xi q_s)_i + \widetilde{\lambda}_1 \widetilde{\gamma}_1 \widetilde{e}^3_1 + \widetilde{\lambda}_1 \delta\epsilon^{G-}_b \\
F^{+}_{3,\,i+1} &\equiv (\xi q_s)^{2+}_{i+1} = (\xi q_s)_{i+1} - \widetilde{\lambda}_2 \widetilde{\gamma}_2 \widetilde{e}^3_2 - \widetilde{\lambda}_3 \widetilde{\gamma}_3 \widetilde{e}^3_3 - \widetilde{\lambda}_3 \delta\epsilon^{G+}_b
\end{aligned}
\tag{D.1}
$$

therefore the solid flux jump corresponding the contact wave placed at the intercell edge can be obtained as:

$$
\begin{aligned}
(\xi q_s)^{+}_{i+1} - (\xi q_s)^{-}_i = &\, \delta(\xi q_s)_{i+\frac{1}{2}} - \\
&- (\widetilde{\lambda}_1 \widetilde{\alpha}_1 \widetilde{e}^3_1 + \widetilde{\lambda}_2 \widetilde{\alpha}_2 \widetilde{e}^3_2 - \widetilde{\lambda}_3 \widetilde{\alpha}_3 \widetilde{e}^3_3) + (\widetilde{\beta}_1 \widetilde{e}^3_1 + \widetilde{\beta}_2 \widetilde{e}^3_2 + \widetilde{\beta}_3 \widetilde{e}^3_3) - \\
&- (\widetilde{\lambda}_1 \delta\epsilon^{G-}_b + \widetilde{\lambda}_3 \delta\epsilon^{G+}_b) = \\
= &\, \delta(\xi q_s)_{i+\frac{1}{2}} - \left[\xi \widetilde{G} \delta(u^3) + \xi \widetilde{u}^3 \delta G \right]_{i+\frac{1}{2}} = 0
\end{aligned}
\tag{D.2}
$$

Hence the solid discharge jump at the edge is null and the intermediate value of the numerical solid flux at the left ant right sides of the intercell edge $i + \frac{1}{2}$ has a constant value $F^*_{3,\,i+\frac{1}{2}}$:

$$
F^{-}_{3,\,i} = F^{+}_{3,\,i+1} = F^{*}_{3,\,i+\frac{1}{2}} = (\xi q_s)^{*}_{i+\frac{1}{2}} \tag{D.3}
$$

The region with constant associated solid flux is represented in Fig. D.24 as a blue color region. This relation ensures that the scheme agrees with

the conservation property for the sediment mass under any condition. It justifies the importance of including a corrector solid flux term when the Exner equation is included into the Jacobian matrix [19].

Considering (D.1) and the strategy proposed in (61) for fixing left-side over-erosion problems, the $\delta\epsilon_b^{G-}$ increase causes a reduction in the intercell numerical solid flux $F^*_{3,\,i+\frac{1}{2}}$. On the other hand, the correction proposed in (62) to fix the right-side over-erosion, i.e. reducing $\delta\epsilon_b^{G+}$, leads to an increment of the numerical solid discharge at the intercell edge $F^*_{3\,|i+\frac{1}{2}}$.